



Title: The neural crest as a bioelectric Rosetta Stone:
translating the analog and digital bioelectric code with Fluorescent Lifetime
Imaging (FLIM)

Authors: McMillen, P.^{1,2}, Levin, M.^{1,2,*}

Affiliations:

¹ Allen Discovery Center at Tufts University, Medford, MA 02155, USA.

² Wyss Institute for Biologically Inspired Engineering, Harvard University, Boston, MA 02115, USA.

*** Corresponding author:**

200 Boston Ave., Suite 4600

Medford, MA 02155

Email: michael.levin@tufts.edu

Running title: Bioelectric Rosetta Stone

Keywords: Bioelectricity, FLIM, Bioelectric Imaging, Neural Crest Cells

Abstract:

Translating the bioelectric code remains one of the core challenges to widespread biomedical translation of bioelectric interventions, as well as a better evolutionary understanding of how developmental ionic signaling became the basis of neural intelligence. Thus, it is essential to develop model systems and protocols in which diverse bioelectrical parameters can be quantitatively studied together, in the living state, and connected to cell- and tissue-level outcomes. Here, we apply state-of-the-art quantitative Fluorescent Lifetime Imaging (FLIM) optical estimation of membrane potential (V_{mem}^{oe}) to map the bioelectric dynamics of spreading *Xenopus laevis* neural crest cells over roughly 18-hour time periods. We identify a slow “analog” bioelectric component that functions on the scale of hours, and a faster “digital” component that acts on the scale of seconds. We then use information theory to show that digital NCC V_{mem} dynamics are largely distinct from calcium dynamics. Finally, we provide a survey of diverse bioelectric events revealing a deep complexity in collective bioelectric dynamics, likely involving tunneling nanotubes in their transmission, which suggests numerous avenues for further investigation.

Introduction

Translating the languages of life

After the fall of their empire, the hieroglyphic language of the Ancient Egyptians was lost to European scholars, hiding from them crucial insights into the foundations of their own more modern culture. The discovery of the Rosetta Stone, a tablet containing a single message written in ancient Egyptian hieroglyphs, ancient Egyptian script, and the accessible language of Greek, allowed them to translate this lost language and access the secrets that it held. Contemporary biologists face a similar challenge to that of 19th century Egyptologists: decoding the ancient languages of our progenitors to better understand ourselves (Figure 1A).

The use of codes is not exclusive to human culture. Biology is replete with encodings, occurring at different size scales and implemented in different types of substrates [1-4]. Advances in bioengineering and regenerative medicine, as well as the basic understanding of evolutionary biology and cognitive science require that we learn to read and write these codes. Our ability to glean information from measurements, and to rationally manipulate molecular and biophysical states, to reliably achieve complex, system-level outcomes in living systems, depends on knowing the mapping between input states and subsequent outcomes.

The purpose of language is to communicate information in a way that increases functional alignment among individuals, and a key early step in translating a language is understanding how information is encoded. This was the central insight of Jean-Francois Champollion, who first used the Rosetta Stone to translate hieroglyphics: "Hieroglyphic writing is a complex system, a script all at once figurative, symbolic and phonetic, in one and the same text, in one and the same sentence, and, I might even venture, one and the same word." (cited in [5]). To understand developmental and regenerative morphogenesis, as well as diseases of cellular cooperation such as cancer, it is essential to characterize the diverse communication pathways occurring among cells and the ways in which cellular interpretation of biophysical states orchestrates functional alignment of cells toward adaptive and consistent anatomical outcomes [6, 7]. Like the hieroglyphic language, we hypothesize that bioelectricity may encode information in multiple different modalities in parallel, showing a tractable and biomedically relevant modality in which physics and semiotics intersect [2, 8].

One particularly interesting physical medium for encoding in living media is bioelectricity. Neuroscience, via its project of neural decoding [9-12], is largely predicated on the idea that mental content—the ability to flexibly navigate a problem space toward adaptive outcomes—is encoded in electrophysiological states. However, bioelectric networks did not first appear in brains—they are an ancient method of encoding and using information, dating back to bacterial biofilms [13] and gaining its full development as a precursor to the control of motility by regulating traversals of anatomical morphospace [14, 15]. We have previously suggested that the binding function that electrophysiology serves in brains—mediating the coordination of large numbers of neurons toward outcomes at the organismal behavior level—extends to (and derives from) developmental biology non-neuronal cells' need to cooperate together toward complex, unified anatomical outcomes [7, 16]. This suggests extension of the neural decoding field [9-12] to other tissues in the body, especially those that are undergoing active pattern formation [16].

Bioelectricity as a primordial cellular language

There is a rapidly growing body of evidence that non-neural bioelectricity plays important roles in development, regeneration, cancer progression, and evolution [17-19] (Figure 1B). Voltage parameters regulate stem cell differentiation [20-24], proliferation [25-29], gene expression [30, 31], and cellular interpretation of canonical biochemical signaling factors [32-35]. Misexpression of ion channels induces ectopic eyes formation in *Xenopus* embryos, even outside of areas competent eye induction by the “master regulator” gene *pax6* [36]. Bioelectricity regulates wing development in *Drosophila* [37], the size of zebrafish fins [38], and the patterning of the vertebrate heart, brain, and face [39-42]. It has also been implicated in evolution of the highly specialized fins of flying fishes [43]. Bioelectric intervention has been shown to rescue regeneration in non-regenerative contexts [44, 45], overcome chemical and genetic teratogenesis [46], and normalize tumor like structures induced by human oncogenes [47-50].

Bioelectricity is also an appealing avenue for biomedical intervention due to the diverse array of interventional reagents that can induce complex, coordinated downstream responses – electroceuticals - many of which are already FDA approved because of their role in neuromedicine and other indications [51, 52]. And yet, predicting outcomes of bioelectric intervention, diagnosis of underlying bioelectric causes of pathology and integration of bioelectricity with the greater cell, molecular and developmental biology knowledgebase has proved challenging due to the daunting technical challenge of observing and interpreting the dynamics of bioelectric patterns at physiologically meaningful timescales. Bioelectricity is a complex computational medium [53] that cannot be controlled by simple 1-to-1 input-to-output relations, and in order to control the bioelectric code, we must be able to read it. Here we report efforts to use the embryonic cell population known as the neural crest as a model system in which to address bioelectrical encoding of developmentally-relevant information [54-57].

The neural crest as a Bioelectric Rosetta Stone

The neural crest is a multipotent stem cell population that sits at the interface between the neural and non-neural paradigms, ultimately differentiating into both neural and non-neural cell types [58-61]. Neural tissue is induced by cues secreted by the notochord, a transient medial organizing structure. Ectodermal cells that receive insufficient inductive cues from the notochord remain non-neural, while cells that receive an intermediate dose become neural crest, which can adopt both neural and non-neural fates. Neural crest cells (NCCs) collectively and intelligently navigate the forming embryo to adopt a diverse variety [62, 63] of fates with cells becoming peripheral neurons, heart cells, melanocytes and cranial bone and cartilage among others. And, especially relevant to our study, they have repeatedly been shown to be bioelectrically active. Amphibian NCCs electrotax toward the cathode of exogenously generated electric fields [64, 65]. Moreover, mutation of multiple key bioelectric effectors prevents normal NCC development, including K⁺ channels [66, 67], calcium channels [68], gap junctions [62, 63], and the mechanosensitive cation non-specific channel Piezo1 [69].

Because of its intermediate state between neural and non-neural cells, we envision the neural crest as a sort of bioelectric Rosetta Stone that may help translate between different aspects of ionic signaling. The Rosetta Stone allowed archaeologists to understand the language of a precursor civilization and, in so doing, to better understand

the foundations of their own more modern culture. Similarly, we propose that bioelectric study of the neural crest will allow us to translate the powerful theoretical and methodological advances of neuroscience to the more ancient functions of non-neural biology, while in turn providing insights into developing insights into primitive cognition that will provide novel insights into the evolution and function of the brain (Figure 1A).

Beyond its appeal as an intermediary between neural and non-neural cell behavior, neural crest cells are an important model for collective cell behavior [70-76]. NCC collectives chemotax towards the attractant Sdf1a, while individual cells are unable to do so[77] demonstrating that the collective is greater than the sum of its parts. Cells expressing a dominant negative version of the Sdf1a receptor CXCR4 regain the ability to chemotax toward Sdf1a when mixed into a collective with wild type cells[77], further evidencing the collective nature of this tissue. NCC collectivity is structural as well as function, as NCCs form supracellular Actin cables that drive migrating collectives *in vitro* and *in vivo* [78].

NCCs demonstrate notable collective intelligence per William James' definition of intelligence as the ability to achieve the same goal via different paths [15, 79]. They show remarkable ability to do so: for example, in response to ablation they can migrate to deficient regions through non-canonical paths [80, 81] (as do neurons [82]), and they can regulate their numbers either up or down, as needed, to achieve correct target morphology [83]. Perhaps most impressively, mouse neural crest cells grafted into chicken embryos can successfully navigate their new environment and successfully form teeth in the chicken's beak [84]. This complex and highly plastic behavioral repertoire points to an underlying complexity and context-sensitive behavior that makes the neural crest and appealing model for studying bioelectric communication and more generally, collective behavior in anatomical state space [85].

Finding the information in the bioelectric code

Neural bioelectric signals are staggeringly fast, complex, and very large in magnitude of the voltage change achieved per unit time. More primitive non-neural bioelectric signals, in contrast, are much slower and weaker in magnitude. Myosin provides a useful analogy for bioelectricity. Muscles contain a highly specialized actomyosin system the facilitates production of macroscale levels of force. A less specialized version of non-muscle myosin pervades eukaryotic biology, driving cell motion and cell and tissue contractility [86]. But while there is a conservation of their molecular mechanism, the tools required to study organismal and cell motility are very different. Similarly, while powerful tools like patch, whole-cell clamping, and multi-electrode arrays (MEAs) have been developed for neural bioelectric signals, the toolkit for reading non-neural bioelectric signals is far more limited [87-89].

Neuroscientists have circumvented these challenges to some degree with calcium imaging, which facilitates relatively non-invasive measurement of long-term measurement of a large number of cells in unison [90, 91]. While bioelectric intervention can alter calcium signals during development [92], it remains unclear how well calcium signaling reflects non-neural bioelectric communication, especially over long periods of time [93]. Specifically, because several other transduction mechanisms leading from voltage change to gene expression changes, besides the opening of voltage-gated

calcium signals, have been studied, it is unlikely that calcium readouts capture the entire richness of cells' responses to endogenous bioelectric events [94].

Evan Miller's group has developed a promising technology that combines their VoltageFluor (VF) dye system with the highly quantitative imaging tool Fluorescent Lifetime Imaging (FLIM) [95, 96]. VF dyes comprise a fluorophore, a molecular wire, and an electron donation quencher (Figure 2A). They insert into the cell membrane like a thumb tack, and once inserted their intensity and fluorescent lifetime change as the direction of the local electric field either pushes the electrons into the fluorophore (hyperpolarization), reducing its intensity and lifetime, or draws them out of it (depolarization), increasing intensity and lifetime. Because lifetime is an intrinsic property of a fluorophore that does not directly scale with dye concentration, FLIM largely eliminates confounds stemming from differential dye incorporation and cell shape changes (Figure 2B-D’'). This is critical for reading non-neural bioelectric signals which tend to be very low magnitude and change over long time-periods, causing them to be easily obscured by even modest artifacts. We use FLIM with the highly photostable far-red VF dye BeRST [97] to enable long-term (>17 hours) bioelectric imaging with minimal phototoxicity and photobleaching for the first time in primary tissue explants.

Here, we seek to uncover ways in which information is encoded in bioelectric signals. Our approach is founded on Claude Shannon's definition of Information [98], which is mathematically similar to the thermodynamic concept of entropy and increases with increasing diversity of states in a system. We discuss the application of Information Theory to biological signal discrimination in greater depth in [99], and apply it to cytoskeletal and calcium signal dynamics in relatively stationary *Xenopus laevis* animal cap explants. Shannon information is highest in systems with high variability, and it follows that such systems are the most appealing candidates as bioelectric communication modalities. Here we extend this methodology to map information flow between previously-undescribed optically estimated V_{mem} and calcium dynamics to migrating neural crest cell explants for an extended time period. We find that, unlike in neurons [90, 91], V_{mem} and calcium dynamics in neural crest are largely independent, revealing a fascinating aspect of the evolution of ionic signaling in multicellular contexts [14, 100-102].

Methods

Frog rearing and mRNA injection

Animal care was done in compliance with and approval from the Institutional Animal Care and Use Committee (IACUC) under protocol number M2023-18 of Tufts University. Capped and tagged mRNA was generated used an mMessage Sp6 *in vitro* transcription kit (ThermoFisher). Embryos were microinjected 4 were injected 4X at the 2-4 cell stage with a bolus of roughly 0.9 μ m outer diameter with mRNA containing 600 ng/ μ L jGCAMP8s mRNA [103], 10 ng/ μ L mCherry-Erk2 [104] and 200 ng/ μ L LifeAct-Turquoise2 [105] in RNase-Free water (Ambion).

pLifeAct-mTurquoise2 was a gift from Dorus Gadella (Addgene plasmid # 36201 ; <http://n2t.net/addgene:36201> ; RRID:Addgene_36201). pHRSFFVp BFP-Erk2 was a gift

from Wendell Lim (Addgene plasmid # 50848 ; <http://n2t.net/addgene:50848> ; RRID:Addgene_50848).

Neural Crest (NC) explanting onto Fibronectin (FN) coated cover glass

NC explant procedure was modified from Gouignard et al., 2021 [106]. NC removal was performed in Danilchick's For Amy (DFA) [107] media to minimize bioelectric effects from multiple media changes. Neural crest explants were removed during neurulation prior to closure of the anterior neural tube (NF stages 15-17). mRNA injection of multiple sensors coupled with rearing at 22°C through gastrulation induces slight heterochrony, and while effort was made to take explants from similarly aged embryos we report a conservatively large stage window. We attempted to mitigate effects of stage variation by cutting 4-5 explants per excised neural crest, pooling and thoroughly mixing the explants in DFA buffer and distributing explants evenly between conditions.

We performed experiments on three separate replicates from distinct clutches of eggs. For each replicate, we changed the spatial location of the three K⁺ conditions to mitigate possible confounds from well location or explant imaging order. It is impractical to confirm the molecular identity of each explanted cell as such testing generally requires either genetically encodable reporters or fixation of the tissue, neither of which is compatible with our analysis. We therefore avoid referring to these explants as 'neural crest cells,' instead using the term 'neural crest explants' to acknowledge the possibility of contamination with, or differentiation into, specific tissue types.

Optically estimated membrane potential (V_{mem}^{oe})

While FLIM greatly improves the quantitative power of bioelectric imaging, as well as allowing monitoring of large numbers of cells, over developmental timescales, all without the disruption of penetrating them with electrodes, it is unreasonable to expect that bioelectric imaging maintains the same magnitude of accuracy as classic electrophysiological techniques in all cell types at all times. Dye internalization, artifacts from dye trapping, V_{mem} -independent effects on lifetime and other unforeseeable artifacts are necessary limitations of the current state of the technology. However, optical estimation does not suffer from the many confounds introduced by comparatively invasive electrophysiology techniques [87]. We use the nomenclature "Optically Estimated V_{mem} " V_{mem}^{oe} throughout this paper to prevent confusion about what exactly we are reporting.

Dye staining

Explants were stained in standard DFA buffer containing 4.5mM K⁺ gluconate, 50uL Nuc Blue reagent (Hoechst 33342, Invitrogen R37605) and 5uL of 0.5mM BeRST DMSO stock (gift of Evan Miller, synthesized by Pharmaron, China) for 30 minutes in a 22°C incubator while being covered from light. Staining media was gradually introduced to 8-well glass bottom chambered coverslips (Ibidi) to minimize disruption to explants and mixed between chambers to minimize uneven staining.

Imaging

Imaging was performed using a Leica Stellaris 8 confocal microscope. Imaging conditions and directory of relevant metadata files (included as supplemental pdf files) is presented in Supplemental Table 1. Long-term imaging was performed at 20°C. For the

quantitative dataset discussed in Figures 3-6 independent replicates were performed with eggs collected from different clutches. 9 total explants were imaged per condition, 3 in each imaging session for the data in these figures. Slight variation due to stage travel rate was present between the three replicates, but because this amounted to only a few minutes over the 17-hour plus duration timepoints between replicates were pooled. Images displayed may be from either 0.5 mM K⁺, 4.5 mM K⁺ or 8.5 mM K⁺ condition unless specified. Some images were scaled up in Fiji without interpolation to make cleaner figures and movies.

Image analysis

LasX FLIM quantification: Curve fitting is performed using the LasX FLIM/FCS module. While Lazzari-Dean et al. [95] use a bi-exponential decay fit for VF2.1.Cl and a mono-exponential decay fit for VF2.0.Cl, we used a mono-exponential fit for all fluorophores due to the relatively low photon counts . For timeseries data reported in Figures 3-6 BeRST lifetime images were binned in LasX prior to exporting to improve curve fitting by increasing photon values per fit, then scaled up in Fiji [108] using bilinear interpolation or in CellProfiler .

Whole-explant quantification: Explant timeseries were exported from LasX as separate intensity and lifetime channels. An intensity factor of 1 per count and a lifetime factor of 0.001 per count were applied so that 16-bit images scaled to picoseconds would be produced for analysis. Unless processed by CellProfiler, binary masks were produced using either the BeRST intensity channel or NucBlue signal.

Kymographs: Kymographs are produced by using the NucBlue signal to mask the channels of interest then running the Radial Reslice tool in ImageJ and producing an average intensity projection. A radius is drawn from Images are formatted as 32-bit with background set to NaN to prevent below-threshold pixels from affecting the data. Positive derivative images are generated by subtracting an image from the image at the next timepoint and discarding any values below 0.

Cell Profiler nucleus outlining: Our CellProfiler [109, 110] pipeline is attached as Supplemental Methods 1. In this study CellProfiler was only used to outline nuclei in Supplemental Movie 7.

Informational analysis of V_{mem}^{oe} and calcium kymographs

The kymographs are cropped to a height of 240 pixels, removing the outermost pixels and binarized with a manually derived threshold, one threshold value being used for all V_{mem}^{oe} kymographs and another for all calcium kymographs. y-axis is then median-binned by a factor of 16 to produce an image 15 pixels high, with the pixels representing average values of a series of concentric circles 16 pixels thick. The x-axis of the resulting kymograph is replaced with time, converting the single kymograph image into a timeseries one pixel thick and 15 pixels high. Both timelapses are then spatially scaled up 100-fold and segmented to make each original pixel into a distinct ROI and a mosaic timelapse with calcium values on the left and V_{mem}^{oe} values on the right created and saved as an .avi format file. The Information Theory software package CAIM [111] was then used to extract timeseries data from each ROI and calculate the Information within each signaling paradigm at each ROI and the Mutual Information between each channel and each ROI.

Data was processed in Excel and statistically analyzed and plotted in Prism. Statistical significance was determined using Friedmann's test with Dunn's multiple comparison test.

Bioelectric event size estimation

Binarized data from the information analysis above was used to estimate the average size of bioelectric events within each explant. The average number of ROIs with signal was measured from each timepoint containing at least one active ROI in either the V_{mem}^{oe} or Calcium paradigm were tabulated, then an average event size for each explant was determined. Explants that did not contain at least one V_{mem}^{oe} event and one calcium event were excluded. Statistical significance was calculated in GraphPad Prism using a paired t-test.

Scan speed bioelectric event dynamic estimation

We observed linear signals perpendicular to the direction of scan speed. We divided the frame capture duration of the image by the number of scan lines composing it to estimate the dwell time for each scan line. We then used ImageJ to draw a line along the masked lifetime image (background pixels being set as NaNs were not included in the analysis) parallel to the scan direction and manually defined to be thick enough to encompass the bioelectric event with minimal contamination from nearby cells. We extracted the variation in lifetime over space using the Plot Profile tool in ImageJ and converted the spatial component to time using the scan line dwell time estimate and plotted the resulting lifetime vs. time plot.

Statistics

Lazic et al. [112], Lord et al. [113], and Motulsky [114] were used as guides for statistical analysis. Multiple neural crests from different animals were cut into smaller explants which were randomized and sorted into different K^+ conditions. Because randomization occurred at the explant level the sample size was calculated as the number of explants, and different explants were used as replicates for statistics. Explants were collected from 3 separate clutches and imaged in three separate sessions with the 3 conditions being imaged in parallel. Out of efficiency concerns we do not explicitly account for possible clutch and imaging session level variability in our statistics, though in Figure 3A we used different colored spots for each of the three replicates. Because long-term timelapses are time consuming, for both information and event size estimation we pool data from all three K^+ concentration conditions to increase statistical power and use color to denote to which condition each datapoint belongs. For the event size estimation explants that do not have both V_{mem}^{oe} and Calcium events were excluded. Statistical tests were conducted using GraphPad Prism 10.4.0 in accordance with its recommendations [114].

Results

As with the characterization of any new information medium or coding modality, use of a model system for cracking the bioelectric code requires knowledge of the kind of bioelectric properties of which it is capable (analog vs. digital signals, signaling “frame rate”, bandwidth in terms of ability to carry different states per unit area, etc.), as well as a knowledge of how these properties respond to stimuli. We examined these in the *Xenopus* neural crest as follows.

Three-dye bioelectric FLIM imaging reveals spatial bioelectric variation obscured in standard non-FLIM imaging

We hypothesized that there exist subtle bioelectric patterns in spreading neural crest explants that are not readily detectable by intensity-only fluorescent imaging. In order to test this, we compared the V_{mem} patterns optically estimated by intensity and lifetime using a set of three bioelectric dyes.

We recently described a strategy [115] to validate specificity of bioelectric patterns detected with BeRST using the control dyes VF2.1.Cl, the lifetime properties have been rigorously quantified with electrophysiology[95], and VF2.0.Cl, a negative control variant of VF2.1.Cl lacking the electron donating quencher that confers V_{mem} sensitivity. We have found that co-staining NC explants with BeRST and VF2.0.Cl dramatically reduces the lifetime and variability of the VF2.0.Cl signal, suggesting a possible FRET interaction between the two dyes (data not shown). We therefore avoided co-staining BeRST with either VF2.1.Cl or VF2.0.Cl, instead staining separate explants in parallel. Conclusions were based on two separate clutches comprising 9 explants stained with VF2.0.Cl, 8 explants stained with VF2.1.Cl and 13 explants stained with BeRST. Imaging conditions were altered slightly between explants to generate comparable images. Explants presented in Figure 2 were not obtained from injected embryos to prevent crosstalk between constructs and VF2.0.Cl and VF2.1.Cl.

Comparison of the intensity (B-C") and lifetime (D-D") components of the three dyes demonstrated the value of FLIM for reading bioelectric states. In the intensity pictures, cell shape appeared to play a major role in apparent V_{mem} . With all three dyes sites of cell-overlap appeared relatively depolarized due the increased local dye concentration generating, a circumferential ring that is not present in the lifetime images. Figure 2B' and C' showing the intensity of the V_{mem} sensitive dye VF2.1.Cl are especially problematic, as they suggested that the central cell clusters are much more depolarized than the individual spreading cells. However, this pattern was also present in panels B" and C" using the V_{mem} insensitive dye VF2.0.Cl, strongly indicating that these patterns are false positives. The FLIM data in panels D' and D" further supported this conclusion as the VF2.1.Cl stained explant has a different pattern from the VF2.0.Cl stained control, which is more uniform. Thus, FLIM removed major sources of noise and reveals subtle bioelectric patterns that this noise obscures.

We observed a few differences, however, indicating possible artifacts. Both VF2.1.Cl and VF2.0.Cl occasionally showed a reduced lifetime in dense clumps of tissue (Figure 3F,G, asterices). This pattern was not present with BeRST, and indeed the opposite tends to be true with dense tissue often having elevated lifetimes consistent with depolarization (Figure 3D",D", E asterisk). One known artifact of VF-FLIM is self-

quenching at high dye concentrations[95]. Due to the density of pre-migratory explants and our desire to do long-term imaging with minimal photon requirements we used BeRST at a relatively high concentration ($5\mu\text{m}$) to increase evenness of penetration. The VF dyes tended to penetrate tissue more effectively than BeRST, meaning that they likely had an even higher local concentration. We interpreted these data to mean that dense tissue tended to be depolarized on the inside and hyperpolarized on the periphery and that this effect is if anything underestimated due to dye quenching artifacts. We also observed that neurites have an elevated lifetime with VF2.1.Cl, indicative of depolarization (D''), while appearing hyperpolarized with BeRST (Figure 2 F''). The hyperpolarization reported by BeRST is more consistent with established biophysical models, suggesting that there is an artifact with VF2.1.Cl, but out of caution we resisted interpreting any neurite patterns in this paper until this contradiction can be resolved.

In (Figure 2E-G'') we have included a gallery of $V_{\text{mem}}^{\text{oe}}$ images of NC explants stained with BeRST and cultured in parallel and imaged roughly 20 hours after plating. FLIM produces two distinct datasets for each pixel. Intensity is a photon count and is the standard readout for fluorescent confocal microscopy. Lifetime is a measurement of the amount of time that the fluorophore remains in the excited state and is reported in nanoseconds. We reported these data in three ways: First, intensity only, which showed patterns as detected by standard bioelectric imaging (Figure 2 E-E''). Second, intensity and lifetime combined, in which pixel brightness was determined by intensity and pixel color is determined by lifetime (Figure 2F-F''). This is the default output of the LasX FLIM module and combines the cell-shape cues provided by intensity, but obfuscates some of the quantitative power of the lifetime data. Third, we have presented the lifetime image masked by the intensity image and colored with a custom LUT (Figure 2G-G''). This presentation technique was the most quantitative and best shows low-magnitude patterns. In figures subsequent to Figure 2 we generally used the lifetime-only presentation technique due to its quantitative power unless otherwise specified.

Together, these data demonstrate that FLIM enabled detection of subtle bioelectric variation that was masked in intensity-only fluorescent bioelectric imaging. Further, they underscore the dangers of ‘false positive’ bioelectric pattern detection with intensity-only imaging that can largely be ameliorated with FLIM. However, they also reveal a remarkable constellation of cell-to-cell bioelectric variation in explanted NCCs, especially in cells that have split off from larger collectives. But how did this variation arise? Were they evidence of transient fluctuations or persistent static cell differences? To address these questions, we leveraged one of the main strengths of bioelectric imaging: the ability to observe large populations of cells in parallel over extended periods of time.

Bioelectric variation in time: NCC explants exhibit multiscale bioelectric signals on scales from seconds to hours

Having identified spatial variation in bioelectric state, we next asked how bioelectric patterns evolve in time during neural crest cell migration and how these patterns respond to bioelectric intervention by altering media K^+ levels. Bioelectric imaging greatly improved the temporal and spatial range over which we could detect bioelectric patterns. We leveraged this sensitivity window to explore V_{mem} dynamics over a roughly 17-hour window as the neural crest explants spread out, migrate collectively, and begin to separate off from their collective to migrate individually.

As we outlined in Figure 1B, one of the greatest challenges in the field of bioelectricity is predicting phenotypic outcomes of bioelectric interventions. Do cells compensate quickly to interventions return to a set V_{mem} , or do they remain de- or hyperpolarized for extended time periods? Are bioelectric dynamics tightly clamped, potentially preventing cells from transitioning into new states, or simply shifted to de- or hyperpolarized levels? To address these questions, we ran parallel longitudinal studies of NCC explants with altered external potassium levels to test the effects of extracellular ion levels on long-term bioelectric patterns. We performed a bulk lifetime analysis on the explant timelapses to estimate global V_{mem} patterns over time by thresholding the Intensity component of the image to remove dim pixels from our analysis. Because this approach does not require image segmentation it is relatively unbiased, but is more sensitive to artifacts like those generated by cell death and dye internalization.

We first wanted to see whether we could detect effects of changing K^+ levels on BeRST lifetime. We determined the average value of each explant over the timecourse and found that, as expected[116], increasing K^+ increased V_{mem}^{oe} (Figure 3A). Unexpectedly, decreasing K^+ levels did not significantly decrease lifetime (Figure 3A). Plotting the mean value at each timepoint suggested that the standard deviation of the 0.5 mM K^+ condition is larger than the other two conditions.

In all three conditions, V_{mem}^{oe} followed a consistent 3-Phase pattern over time (Figure 3B). When the data from all three conditions are pooled each phase was statistically distinct from its previous phase. Initially the explants appear relatively depolarized, followed by a roughly 6.5 hour period of gradual hyperpolarization. This depolarization generally manifested as bioelectric gradient with the center of the explant appearing relatively depolarized with increased polarization towards the explant periphery (Supplemental movie 1). This central depolarization tends to flatten during this 6.5 hour period as the explant hyperpolarizes. The initial hyperpolarization window is followed by gradual depolarization over the next 10 or so hours, with Phase 3 not being significantly different from Phase 1.

Phase 2 and 3 explants in 8.5 mM K^+ had significantly higher V_{mem}^{oe} than explants in 4.5 mM K^+ , while in Phase 1 none of the conditions were significantly different (Supplemental Figure 1). This pattern was evident in Figure 2B, as the gap between the mean of the 8.5 mM K^+ explants and the 4.5 mM K^+ explants starts small in Phase 1, expands in Phase 2 and remains large in Phase 3. These trends were consistent with an intrinsic variation in K^+ permeability as cells progress through migration.

To better explore the unexpected lack of V_{mem}^{oe} reduction in the 0.5mM K^+ condition, and informed by the relatively large standard deviation in this condition (Figure 3D) we examined the long-term dynamics of each explant independently (Figure 3D-F). These independent observations revealed relatively short, sharp depolarization events that are most prominent in the 0.5mM condition (Figure 3D, red asterisk) and seem most evident during Phase 2. Because these signals were relatively rapid (minutes) and appeared to be discrete events, as defined by a changing time much faster than the duration of the constant periods between, we refer to them as ‘digital’ to differentiate them from the slow (on the order of hours) ‘analog’ bioelectric signals. These signals confounded attempts to determine the resting membrane potential of cells in the 0.5 mM K^+ condition, explaining the high standard deviation in this condition and potentially explaining why it does not have significantly lower V_{mem}^{oe} than the 4.5mM K^+ condition.

Closer qualitative analysis of these digital signals revealed that they often involved a large number of cells, but did not necessarily encompass the entire explant. In the example low K⁺ treated explant in Figure 4A and B has split into two fragments (see Supplemental movie 1 for full video). In Panel B, the bottom fragment depolarized as a collective while the upper fragment remained relatively constant. 14 minutes later, in panel H, the upper fragment collectively depolarized while the lower fragment gradually hyperpolarized. This trend suggested that these two fragments contain separate dynamic bioelectric circuits. We have also provided two more examples with combined V_{mem}^{oe} and intensity to show the diversity of digital bioelectric signals (Supplemental Movies 2 and 3).

Taken together, these data revealed a slow, 3-phase progression of V_{mem}^{oe} during NC explant spreading: an early, relatively depolarized phase characterized by a depolarized center that gradually becomes more hyperpolarized toward the periphery (Phase 1), a second more hyperpolarized phase in which this gradient weakens during which cells begin to separate from the explant (Phase 2), and third phase of increasing depolarization (Phase 3). Together these data suggested that membrane K⁺ permeability shifts as NCC migration progresses. Finally, we identified an unexpected increase in fast, short duration depolarization events in the low K⁺ condition, demonstrating that even very simple bioelectric interventions may have nonlinear phenotypic consequences.

Digital bioelectric dynamics partially overlap with calcium dynamics

In neurons, calcium dynamics are strongly correlated with depolarization [90, 91]. We compared V_{mem}^{oe} and calcium patterns in order to determine if this is true in the NC as well.

Calcium signaling is one of the best-studied dynamic signaling paradigms in non-neuronal biology [117, 118], and it has regularly been used as a proxy for dynamic neural signals for decades [90, 91, 119]. It has further been found to be active during NC explant migration and patterning [120, 121] and disruption of the Ca²⁺/H⁺ channel AMO1 [68], and the nonspecific cation channel Piezo1 prevents normal NCC migration *in vivo* [69]. Given this correlation between dynamic neural signals and calcium, we hypothesized that the digital bioelectric signals we describe in the previous section are an undescribed component of the dynamic non-neuronal calcium paradigm.

We analyzed our timeseries for evidence of correlation between bioelectric and calcium signals, and as we hypothesized, we found examples of calcium signals that correlate with bioelectric signals (Figure 4C). However, we also observed bioelectric events with no corresponding calcium signal (Figure 4D) and calcium signals without corresponding bioelectric signals (Figure 4D). Given these data, we rejected the hypothesis that calcium can be a sufficient proxy for developmental bioelectricity, and instead concluded that bioelectric and calcium signals are crosstalk with one another, but lack the tight correlation canonically found in neural bioelectricity.

To more holistically compare calcium and digital bioelectric dynamics we turned to kymography (Figure 5 A-O). Because analog and digital bioelectric signals differ by the relative rate of their signal changes, we deconvolved them by creating ‘positive derivative’ timeseries by subtracting the V_{mem}^{oe} lifetime (or calcium intensity) values at each timepoint from the following timepoint. Kymographs produced from the undifferentiated

image (Figure 5 D,H,L) showed the analog system dynamics, while kymographs of the positive derivative image reveal the digital dynamics (Figure 5 E,I,M).

We generated positive derivative timeseries by using the NucBlue nuclear signal to mask the timeseries and remove all datapoints outside of the nucleus ROI. This thresholding served two purposes: it removed much of the internalized dye that accrues within cells over time as the vesicles housing this dye tend to be occluded by the nucleus, and it removed noise from cell movement which is a substantial confound for this positive derivative approach. We also used nuclear thresholding with the original images. We then used the “Radial Reslice” tool in Fiji [108] to draw 360 kymographs (spaced 1 degree apart) spanning the center of the image to its periphery (Figure 5A,B). Stacking these 360 kymographs into an average intensity projection produced a single image that conveys dynamic information about the bioelectric evolution of the whole explant in space and time.

We show representative kymographs from our three conditions in Figure 5 D-O. The analog trends visualized by the undifferentiated kymographs aligned with the trends we described in our whole-explant analysis (Figure 3): Initial depolarization followed by hyperpolarization that eventually trended back to depolarization, a depolarization to hyperpolarization gradient from the center of the explant to the periphery that gradually faded, and a strong hyperpolarization in peripheral cells splitting off from the explant. The effects of external K⁺ levels also aligned with the low K⁺ condition demonstrating stronger hyperpolarization during Phase 2 and the 8.5mM K⁺ condition demonstrating higher depolarization in Phase 3.

Examination of the kymographic datasets lead us to formulate two hypotheses: (1) that V_{mem}^{oe} and calcium dynamics were weakly coordinated in migrating NCCs and (2) that V_{mem}^{oe} dynamics tended to be larger in scale than calcium dynamics. To quantitatively evaluate these hypotheses we applied well-established Information Theory formalism using the tool CAIM (**C**alcium **I**maging) [111], which we have previously used to quantify Information flow in and between the calcium and cytoskeletal pathways in *Xenopus laevis* animal cap cells[99].

We began by pooling V_{mem}^{oe} and calcium data from the 0.5mMK⁺, 4.5mMK⁺ and 8.5mMK⁺ conditions in an attempt to estimate the Informational properties of these pathways throughout the spectrum of K⁺ levels they may encounter during development and improve our statistical power. We determined an average information value for each explant. In this pooled data we detect an average of 0.079 bits of Information in the V_{mem}^{oe} pathway and 0.062 bits detected in the calcium pathway (Figure 6B) though these values are not significantly different.

Only about 7% of calcium Information is shared with V_{mem}^{oe}

To test our hypothesis that calcium and V_{mem}^{oe} and calcium are weakly correlated in migrating NCC explants we measured the Mutual Information between the two variables within each ROI and compared it to the amount of Information measured in each pathway. Consistent with our hypothesis Mutual Information between calcium and V_{mem}^{oe} was significantly lower than either of the two variables (Figure 6B), only about 7% of the Information measured in the calcium pathway and 5.6% of the Information measured in V_{mem}^{oe}. These data suggest that the two pathways are largely, though not entirely, independent in migrating NCCs.

V_{mem}^{oe} events tend to be larger than calcium events

We observed that V_{mem}^{oe} events tend to be incorporate more cells than calcium signaling events. To test this, we used the binarized ROI data generated for the CAIM analysis above and measured the average number of ROIs included in events of each signaling paradigm. Explants not exhibiting both calcium and bioelectric events were excluded from this analysis, and the number of events was not considered, only the average size of the detected events. Each datapoint represents the average event size for the indicated paradigm for one explant, and the K^+ condition to which the explant belongs is indicated by the datapoint color.

Survey of rare bioelectric events implies cytological bioelectric decision making

The expanded spatial and temporal range of bioelectric imaging (Figure 2D) allows us to capture relatively rare events that would be extremely challenging to catch with classic needle-based electrophysiology. The relative rarity of spontaneous occurrence of these events has prevented us from drawing quantitative conclusions about them at this time, but should provide a foundation for future study while underscoring the fascinating complexity of the bioelectric world.

V_{mem}^{oe} increases during cell division

Bioelectricity has been implicated both phenomenologically and functionally in many aspects of the cell cycle [28, 122-124]. In Supplemental Movie 4 we document several events of depolarization during cell division, one of which is shown in Figure 7A. This observation aligns with previously described bioelectric cell cycle patterns [125], reinforcing the ability of the VF-FLIM technique to detect previously established bioelectric events. Further, the minimal invasiveness of bioelectric imaging coupled with its high temporal and spatial resolution provides an appeal platform to tease apart the bioelectric mechanisms of cell cycle progression.

Cells and cell collective depolarize upon re-encountering their original collective

In Supplemental Movie 5, we observed a cell hyperpolarize, break off from the collective, and migrate independently before contacting another location in the explant, depolarizing (Figure 8B), and integrating into this new location. Contact appears to be mediated by tunneling nanotubes [121, 126-132]. We have also observed this phenomenon with cell collectives, which depolarize in unison when the most proximal member of the group re-contacts the greater collective Supplemental Movies 6 and 7. This immediate, long distance response points to a role for contact-mediated bioelectric signaling in balancing the rate and degree of spreading during NCC migration, though further study will be needed to evaluate its functionality.

Scan artifacts reveal dynamic signal kinetics

We have observed that in explants raised for roughly 22 hours at 18 degrees, switching from 4.5mM K^+ to 0.5mM K^+ appears to stimulate bioelectric signals similar to those observed in Phase 2 of imaged over time at 20 degrees. We leveraged this observation to survey for fast bioelectric events at increased magnification (Supplemental movies 2 and 3). Under these conditions we occasionally observed straight lines of

depolarization perfectly parallel to the y-imaging axis. Because we are performing line-scanning imaging we interpret these lines as digital bioelectric events that manifest between successive scan lines. Assuming that these bioelectric events are consistent across the cell we can use the line-scan rate across an ROI parallel to the x-axis to estimate the kinetics of the bioelectric signal. We find that these signals can be repetitive and have relatively fast on-kinetics and slow off-kinetics (Figure 9C',C''). The frequency of these signals varies from cell-to-cell, suggesting a diversity in the underlying ion channel mechanism, though they tend to persist for on-the-order of seconds. Notably the cell in C' was in direct contact with several neurite-like projections, presenting the possibility that neuronal activity may play a role in producing or modulating some of these digital bioelectric signals.

Strikingly, we found that these digital bioelectric events can span long ranges in cell collectives, and even propagate to cells outside of the core collective and presumably linked only by tunneling nanotubes (Figure 7C''). By assuming uniform activation across the collective in this case we can estimate the collective digital bioelectric signal kinetics and find a third bioelectric pattern distinct from the ones in C' and C''. The diversity in on and off kinetics of these signals provides a tantalizing glimpse into the temporal encoding of non-neural bioelectric events, though the relative rarity of these events precludes deeper interpretation without further experimental optimization.

Bioelectric activity of NC explant projections

Because it stains the cell membrane, BeRST effectively highlights tunneling nanotubes and other cellular projections that have a high ratio of cell membrane to cytoplasm. Such projections have been shown to be able to mediate long-distance communication [129], including bioelectric communication via gap junctions [126, 128]. In rare cases like that shown in Figure 7D we observed that depolarization of the cell body extends to its tunneling nanotubes. Notably the tunneling nanotubes of multiple cells depolarize in unison suggesting that the bioelectric reach of the cell collective is much greater than the space occupied by the cell bodies might suggest. This is consistent with our finding of relatively high mutual information in the V_{mem} pathway compared with the calcium pathway. More generally the small size of tunneling nanotubes makes them exceedingly difficult to clamp with existing technology, and this finding demonstrates that bioelectric imaging may be a powerful tool for better understanding their dynamics.

Discussion

The Rosetta stone's value stemmed primarily from its revelation of both similarities and differences between ancient and modern languages. Likewise, we analyze NCCs to reveal both similarities and differences between neural signaling and non-neural and neural bioelectric signals. We describe some key pitfalls in bioelectric imaging and discuss how FLIM can be used to circumvent them. We then describe long-period analog bioelectric patterns that manifest over the course of hours and much faster digital bioelectric signals that manifest on the order of seconds. We then apply information theory to demonstrate that, unlike action potentials[90, 91], these digital bioelectric signals are mostly distinct from calcium dynamics. Finally, we discuss the implications for these comparisons to the ontogeny of neural bioelectricity.

The value of FLIM in revealing bioelectric patterns

Perhaps the most generally applicable finding of this paper is the danger of using intensity-only measurements to detect bioelectric patterns. The high level of confounding noise both obscures subtle bioelectric patterns (compare Figure 2C' and 2D') and, even more problematically, can appear as false-positive signal (compare Figure 2 C'' and D''). Due to the necessity of long-term imaging for our approach, we were limited in our ability to detect contamination from NCC-proximal tissues or differentiation of multipotent NCCs into any of the many types of cells to which they give rise. Our work reveals a striking variety in bioelectric signals during NCC migration and provides a foundation for future studies to deconvolve the phenomenological and functional nature of contributions of inter-tissue interactions, cell differentiation and crosstalk between different NCC derivatives to the NCC bioelectric code. Applications of understanding the roles of ionic signaling for orchestrating cell behavior more broadly extend across evolutionary developmental biology [102, 133], the biomedicine of birth defects and injury [41, 134, 135], and the use of diverse cell types in programmable biorobotics [136].

The analog bioelectric code

Migrating explanted cells follow a slow three-phase bioelectric trajectory that manifests over a series of hours. (Figure 3A-G, Supplemental Movie 1). In Phase I a strong gradient with more depolarized cells on the inside and more hyperpolarized cells on the outside. In Phase II this gradient weakens as the whole explant hyperpolarizes and begins to break apart. Finally, in Phase III the explants again depolarize. While these trends are consistent, the actual estimated bioelectric values vary considerably between explants indicating a lack of fixed gating setpoints lead us to refer to these as "analog" signals.

Effects of K⁺ concentration on bioelectric dynamics of NCC explants

How do bioelectric interventions affect bioelectric signals? One of the biggest challenges in the field of bioelectricity is designing bioelectric interventions that reliably produce desired phenotypic outcomes (Figure 1). Doing so is necessary for therapeutic intervention in regeneration and cancer treatment [137, 138]. Here, we took steps to bridge this gap by measuring the effects of a common bioelectric intervention, variation of extracellular K⁺ levels, over an extended period of time. As predicted from previous

work [116], elevating extracellular K⁺ appears to depolarize cells. Reducing K⁺ does not significantly hyperpolarize cells, however. We further found that reduction of extracellular K⁺ lead to an unanticipated increase in fast ‘digital’ bioelectric signals demonstrating that even simple bioelectric interventions can have major non-linear effects. The mechanisms by which reduced K⁺ could increase digital bioelectric signaling remain unclear, though it is of some interest that reduced K⁺ in the brain has been associated with sleep [139], and thus our findings may have implications for the primitive evolutionary origins of sleep.

The digital bioelectric code

What role could digital bioelectric signals play? There is a growing body of evidence that temporally encoded signaling dynamics are an underappreciated element of signal transduction, with pulsed and static inputs of the same growth factor having different effects. [140-143]. Given that neural bioelectric signals are fundamentally digital, it follows that their more primitive non-neural counterparts would also have temporally encoded properties. The variable off and on kinetics we report in Figure 7C provide evidence for the tantalizing possibility that there may exist a temporally encoded vocabulary of non-neural digital bioelectric signals. While the rarity of these events limits our ability to study them, future work better characterizing may go a long way to addressing our key knowledge gap of designing bioelectric interventions to achieve specific outcomes.

There is also some evidence of this phenomenon in bioelectric signaling. Elegant work employing fluorescence-fluctuation correlation analysis of the genetically encoded voltage-indicator rEstus has shown that V_{mem} fluctuations can correlate between cells in immortalized A375, HEK293T and MCF cell lines, and they report reduced V_{mem} variation in confluent clusters[144]. The events that we describe are more discrete than the fluctuations describe by Rühl et al. [144], and while we see spatial variation increase in isolated cells, cells within collectives reliably produce robust digital signals. Further work will be needed to determine if the digital bioelectric signals that we report are alternative manifestations of the same phenomenon described by Rühl et al. or if they are separate pathways.

How does digital V_{mem} and calcium signals compare in NCCs? Calcium and V_{mem} are largely distinct informational channels in NCC explants, in a substantial departure from the neural paradigm (Figure 8). This disparity highlights the danger of using calcium as a proxy for V_{mem} in non-neural cells and underscores the importance of calcium-independent effectors of bioelectric signals. V_{mem} signals exhibit mutual information at a greater distances than calcium signals. This patterns aligns interestingly with the specialized function of these channels in neurons, in which V_{mem} allows for fast long-distance communication while calcium mediates the relatively local process of vesicle release. Could the long-distance nature of the bioelectric signals that we see point to an intermediary evolutionary mechanism that was supplanted by axons in the brain? Better understanding the mechanistic origins of NCC digital signals may provide insights into the early evolution of neural bioelectricity.

What is the molecular basis of digital bioelectric signals? Hyperpolarization activated cyclic nucleotide gated channels (HCN) increase membrane cation conductivity in response to hyperpolarization and have been shown to mediate long-range repair of chemical and genetic perturbation of *Xenopus* development [46, 145, 146]. These

channels are known to function in stem cells [147-149], excitatory cells including neurons [150] and cardiomyocytes [151, 152], making them reasonable candidates for effectors of the digital bioelectric signals we describe here. However, HCN channels are calcium permeable, and digital bioelectric signals only loosely correlate with calcium dynamics. Likewise, while the mechanosensitive nonspecific cation channel Piezo1 is necessary for proper NCC migration [69], it too show allow calcium influx and thus it is an unlikely effector for digital bioelectric signals. Our data therefore point to an alternative hyperpolarization activated ion channels that can coordinate cell physiology over large distances making these appealing targets for future studies of repair and regeneration.

Implications for the deep history of bioelectricity

Comparison of the bioelectric circuitry of comparatively primitive NCCs with the more specialized, highly stereotyped circuitry of action potentials provides a tantalizing glimpse into the early ontogeny of neuron specification. We show here that calcium and V_{mem} dynamics have distinct computational capacities in neural crest cells, suggesting that they existed as distinct phenomena very different from their textbook roles in neurons during deep evolutionary time. Could some happy accident of the kinetics of the circuitry produced by their unification be the spark that enabled evolution of the neuron and all that followed? If so, a similar non-linear increase in computational power may be synthetically attainable through directed engineering of other biological circuitry. Further understanding the computational properties and semantics [1, 2, 8, 53, 153-158] of the bioelectric code in both neural and non-neural cells will be foundational to the development of a synthesis of behavioral and morphogenetic problem-solving in biology, and the novel forms of computation it has the potential to unlock.

Acknowledgements

We gratefully acknowledge support via Grant 62212 from the John Templeton Foundation and of a sponsored research agreement from Astonishing Labs. We thank Evan Miller for his kind gift of VF2.1.Cl, VF2.0.Cl and BeRST dyes, Erin Switzer for Animal Husbandry support, Daniel Tom and Giulia Ossato for training with FLIM, and Julia Poirier for help with the manuscript.

Figures:

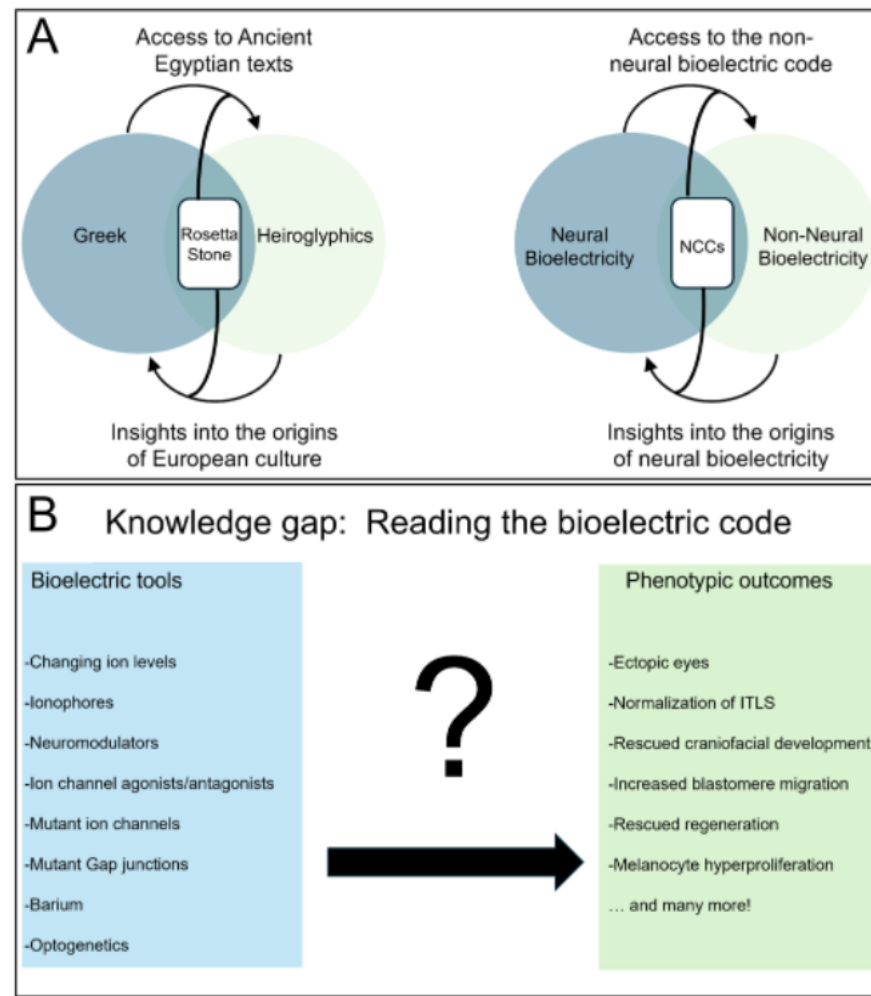


Figure 1: Using the neural crest as a bioelectric Rosetta Stone to translate the bioelectric code

- (A) As Europeans used The Rosetta Stone to translate between the Greek and Ancient Egyptian languages, we aim to use the neural crest to better understand both neural and non-neural bioelectric communication.
- (B) Bioelectric Imaging fills the key knowledge gap between bioelectric interventions and outcomes.

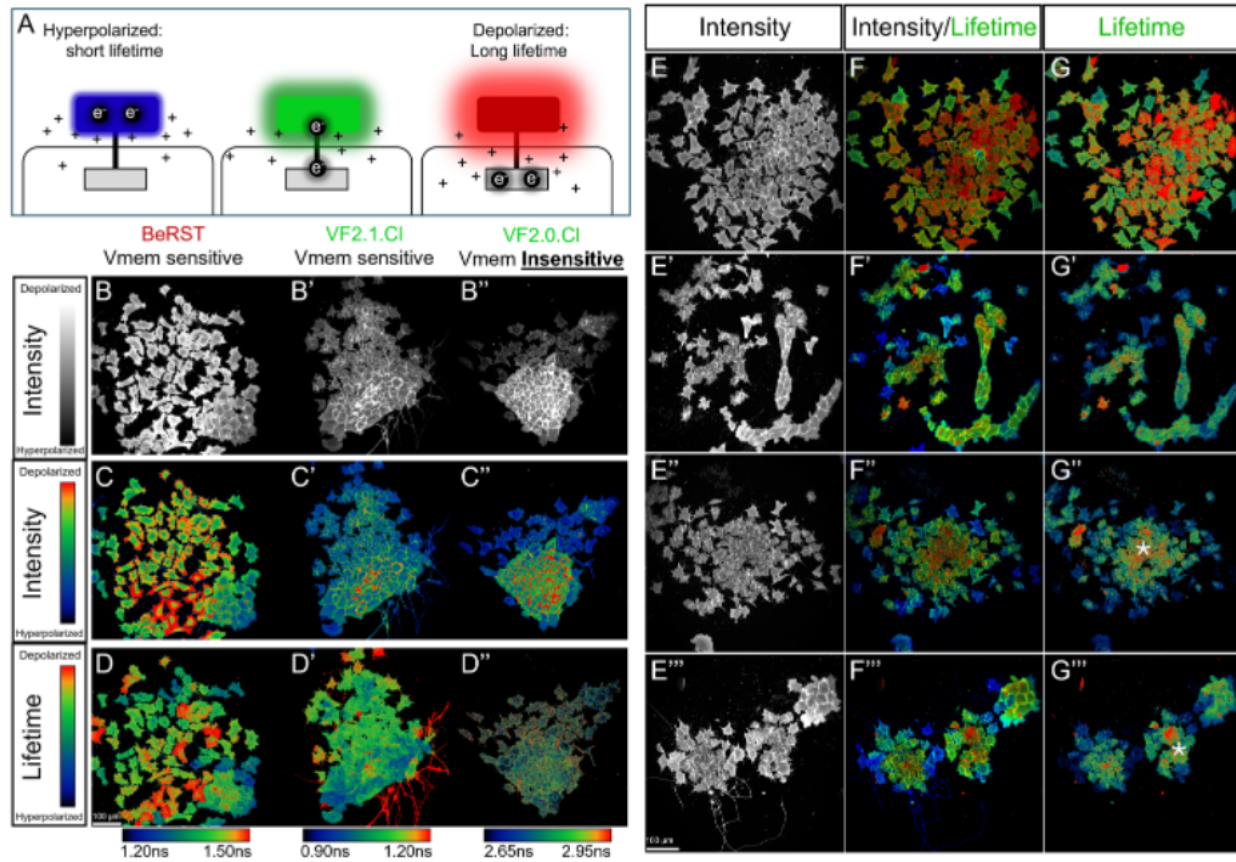


Figure 2: Neural crest explants exhibit remarkable spatial bioelectric variability

(A) In VoltageFluor dyes quenching electrons reduce fluorophore intensity and lifetime when loaded into hyperpolarized cells. In depolarized cells, the electrons are drawn out of the fluorophore, the quenching is relieved and both the intensity and lifetime of the dyes are increased.

(B-D) Gallery of NC explants near the end of spreading, roughly 22 hours after explanting raised at 18° C.

(B-B'') Intensity-only images of the type produced by non-FLIM confocal fluorescent imaging.

(C-C'') Intensity/Lifetime composite images in which intensity is reported by pixel brightness and lifetime is reported by pixel lifetime.

(D-D'') Lifetime only images with background removed via masking using the Intensity only image.

(E-G) Representative control explants comparing V_{mem} sensitive and V_{mem} insensitive VF dyes.

(E) BeRST, which is the dye used throughout the rest of this paper. Asterix shows dense tissue fragment which shows no sign of dye-density dependent quenching.

(F) VF2.1.Cl, a green dye that has been rigorously quantified with FLIM[95]. Asterix shows dense fragment with evident dye-density dependent quenching.

(G) VF2.0.Cl, a V_{mem} -insensitive control variant of VF2.1.Cl lacking the quencher that confers V_{mem} sensitivity. Asterix shows dense fragment with evident dye-density dependent quenching.

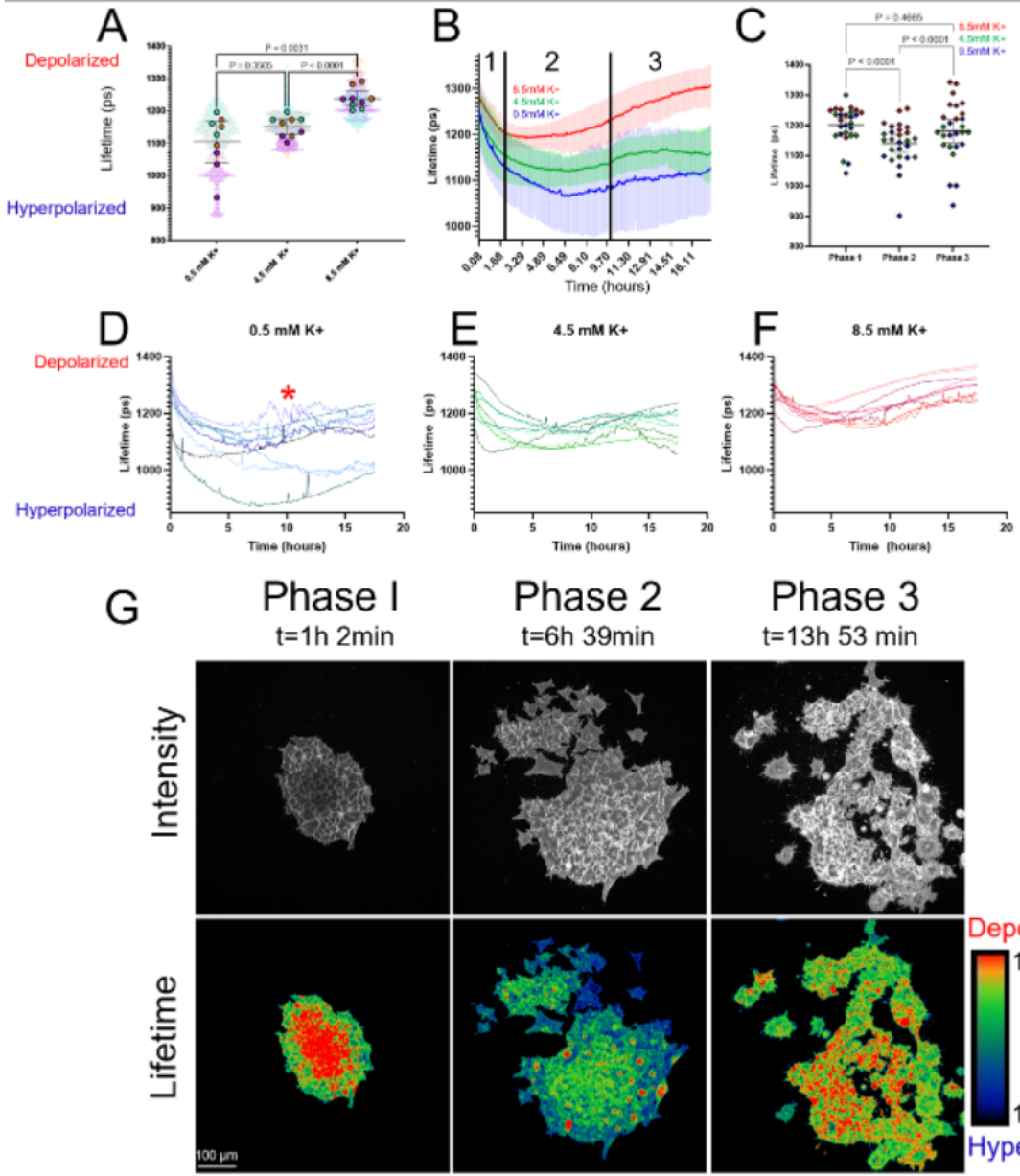


Figure 3: NC explants exhibit a three-phase pattern of long-term analog bioelectric changes

(A) Increasing K^+ by 4mM increases V_{mem}^{oe} , while decreasing K^+ by 4mM does not decrease V_{mem}^{oe} . Significance determined using Browne-Forsythe and Welch ANOVA tests with Dunnett's T3 multiple comparison test in Prism. Large datapoint represent average values over the complete timecourse for a single explant (used to determine statistical significance), and small datapoints represent individual timepoints. Different colors represent different clutches. Plot produced following [113]. Line at mean, Error bar = 95% confidence interval.

(B) Mean whole-explant lifetime over time displayed with SD. Vertical lines demarcate Phases.

(C) V_{mem}^{oe} decreases from Phase 1 to Phase 2, then increases from Phase 2 to Phase 3 in timeseries pooled from all 3 K^+ conditions. Datapoints represent mean V_{mem}^{oe} values of a single explant during indicated Phase. Datapoint color indicates K^+ condition. Significance determined with repeated Measures One-Way ANOVA with Tukey's multiple comparison test in Prism. Line at mean, Error bar = 95% confidence interval.

(D-F) Traces of individual explants raised at different K^+ concentrations over time. Asterisk in D indicates increased dynamics during Phase 2 in 0.5 mM K^+ condition.

(G) Representative image of NC explant raised in 4.5 mM K^+ at the three different bioelectric phases.

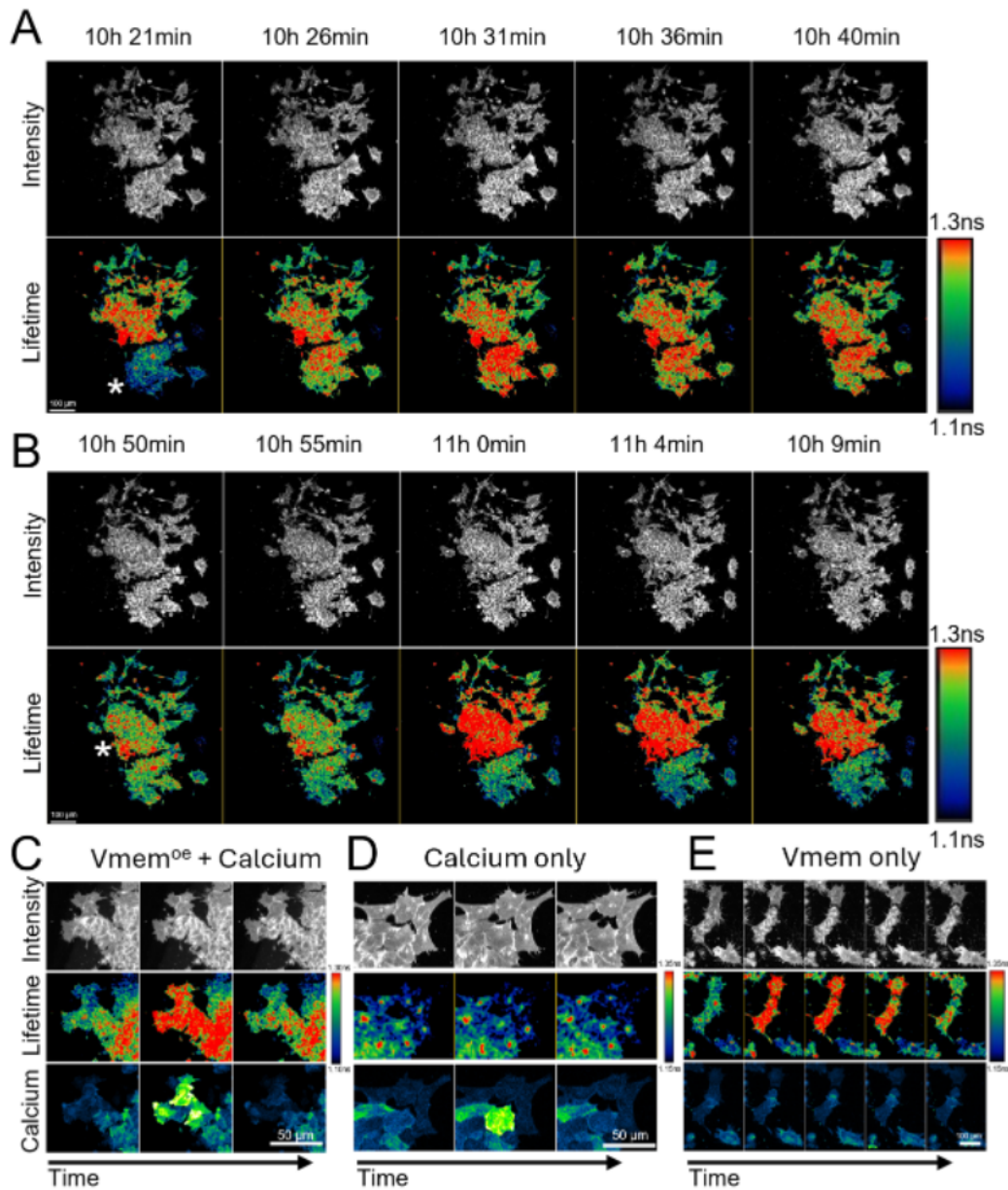


Figure 4: NC explants exhibit multicellular digital signals on the scale of minutes that only partially correlate with calcium signaling

(A,B) Successive frames of intensity and lifetime images showing digital bioelectric signals in NC explants. Asterisks indicate which fragment of the explant depolarizes during the timeseries.

(C,D,E) Successive timepoints of BeRST intensity, V_{mem}^{oe} and jGCaMP8S reported calcium dynamics. In C the apparent depolarization coincides with a calcium signaling event, though not all depolarized cells exhibit a calcium response. D shows a calcium event with no corresponding bioelectric event. E shows a bioelectric event with no corresponding calcium event.

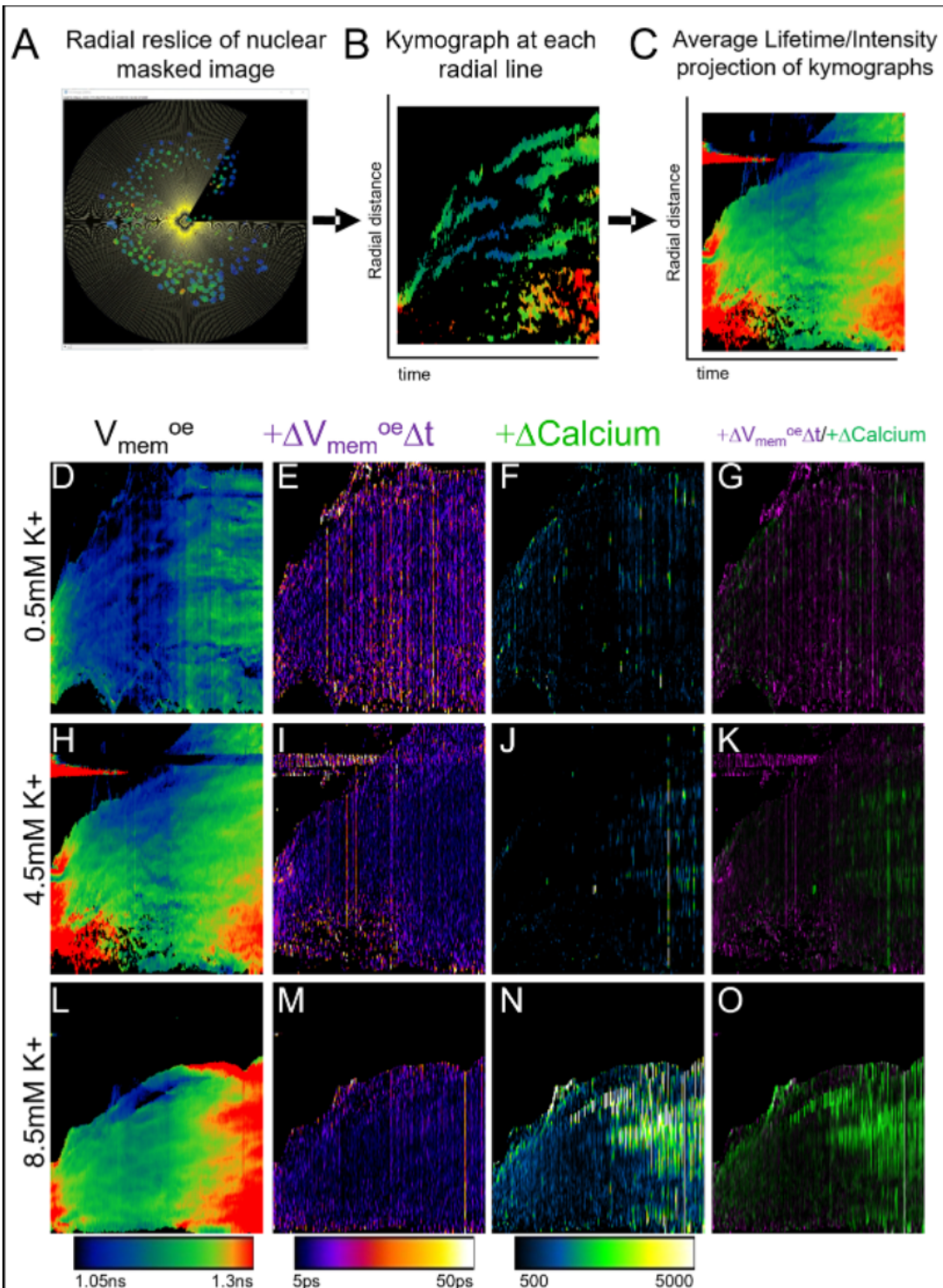


Figure 5: Kymograph analysis reveals distinct analog and digital bioelectric signals
 (A) Screenshot of radial reslicing of a lifetime image after application of a nuclear mask generated from Nuc Blue DNA stain signal.
 (B) Resultant kymograph of a single radial spoke.

(C) Average intensity projection combining lifetime values at each radial spoke to produce a composite representation of bioelectric activity in kymograph space.

(D-O) Representative kymographs of V_{mem}^{oe} (D,H,L), the positive derivative of V_{mem}^{oe} (E,I,M) and calcium (F,J,N) and a merge of V_{mem}^{oe} and calcium (G,K,O) at different K^+ concentrations.

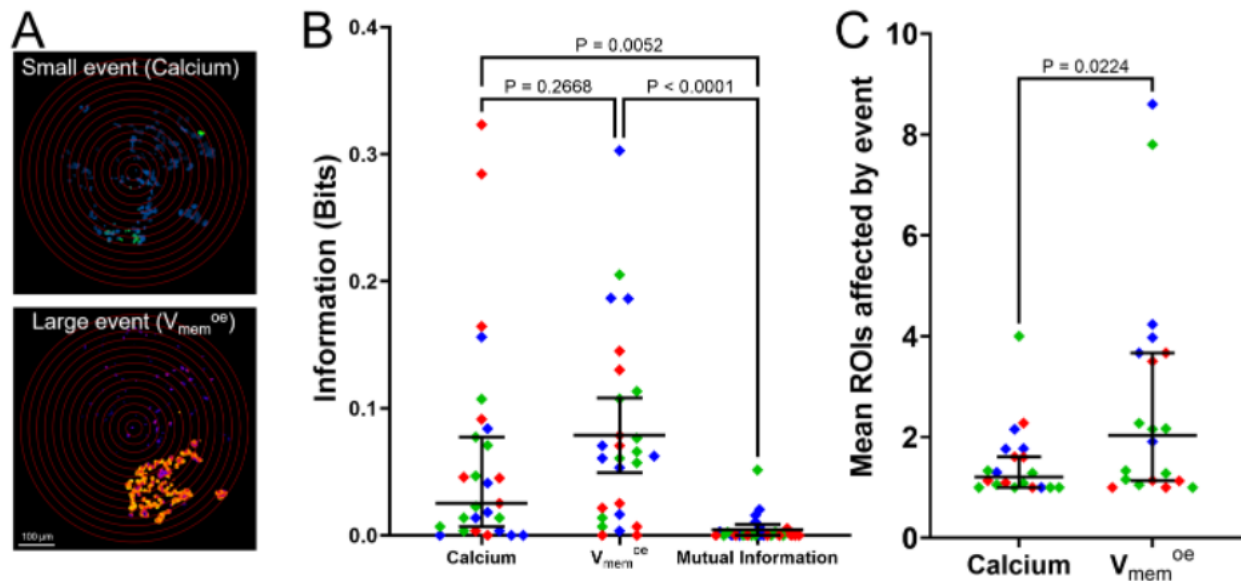


Figure 6. Information analysis of calcium and V_{mem} channels shows they are distinct paradigms that respond differently to changes in resting membrane potential

A. Movies are segmented into 15 concentric circles that are then used as ROIs for Information (B) and object size analysis (C). Small events intersect a small number of circles producing low Mutual Information values (A), while larger events cross many circles to give high Mutual Information values (A').

B. The information contained in both the V_{mem}^{oe} and Calcium paradigms is greater than the mutual information between them (Friedman test with Dunn's multiple comparison post-test) Line at median, error bars = 95% confidence interval.

C. Bioelectric and calcium events were scored by the mean number of ROIs affected to estimate event size. Events without at least one bioelectric and calcium event were omitted. Significance determined via paired t-test to compare event size within each explant. Line at median, error bars = 95% confidence interval.

Values for B and C were obtained by pooling datasets with spot color signifying K^+ level: 0.5 mM K^+ (blue), 4.5 mM K^+ (green) and 8.5 mM K^+ (red).

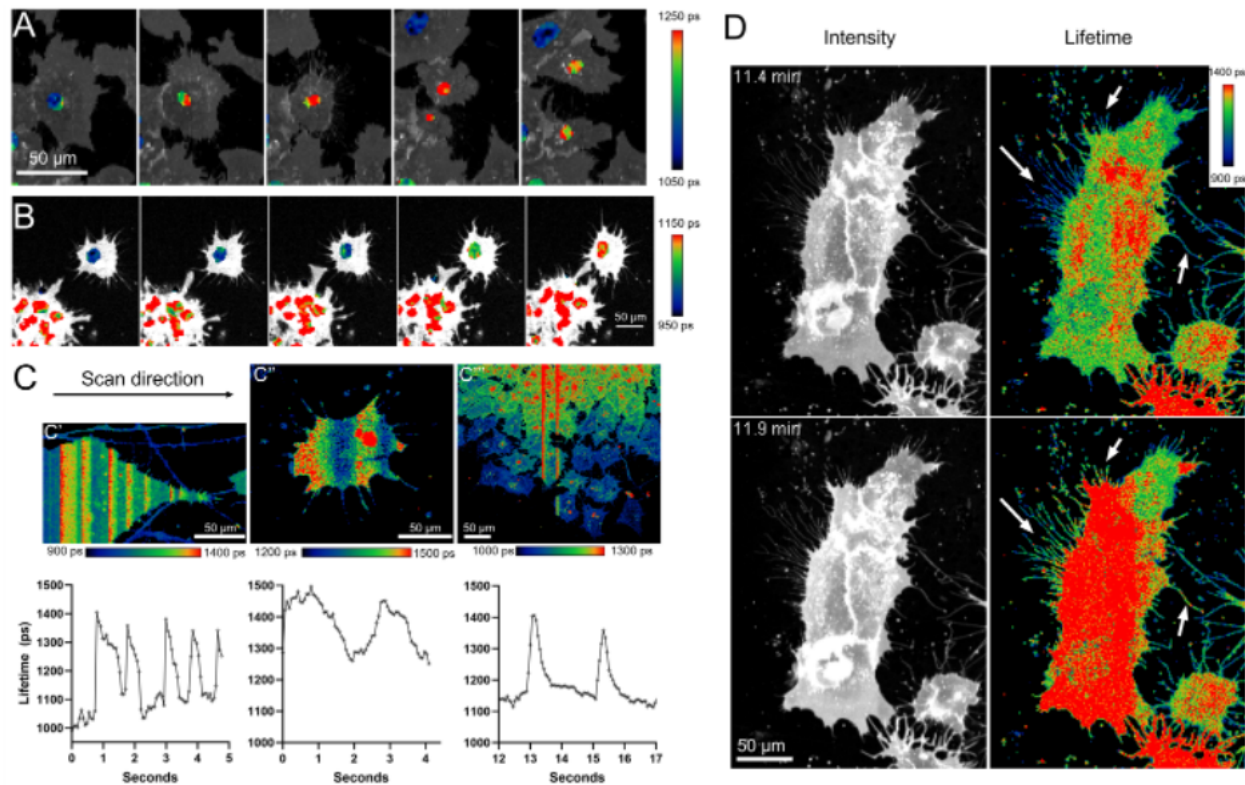


Figure 7: Survey of rare bioelectric events

(A,B): NucBlue signal was used to separate the nucleus ROI from the cell body. BeRST FLIM is shown in the nucleus ROI while BeRST intensity is shown in the cell body to show V_{mem}^{oe} and cell shape clearly at the same time.

(A) Depolarization prior to cell division

(B) Depolarization of isolated cell upon re-contacting collective

(C) Measurement of vertical scan-line artifacts facilitates estimation the kinetics of bioelectric events.

(D) Cellular projections appear to depolarize in concert with cell bodies.

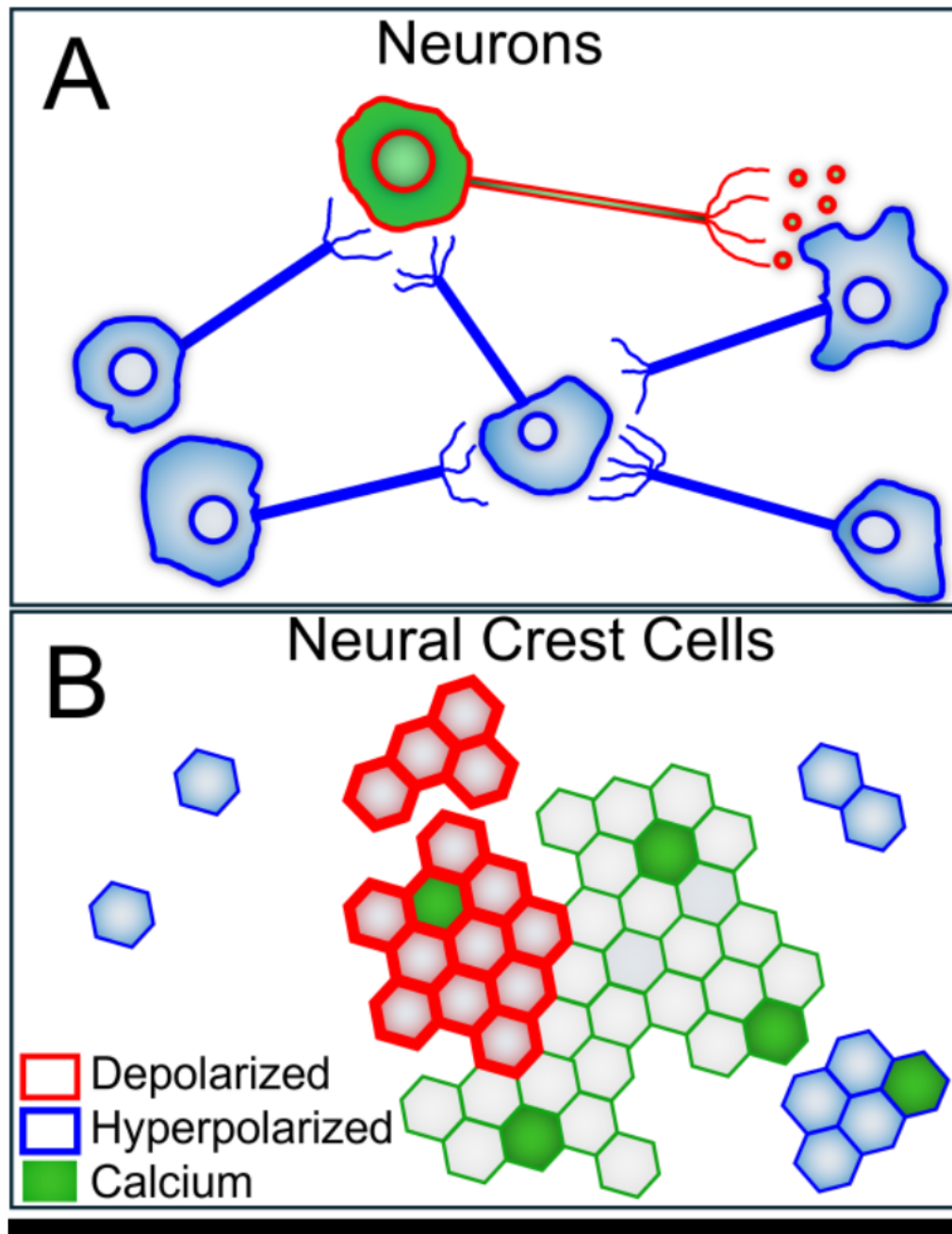
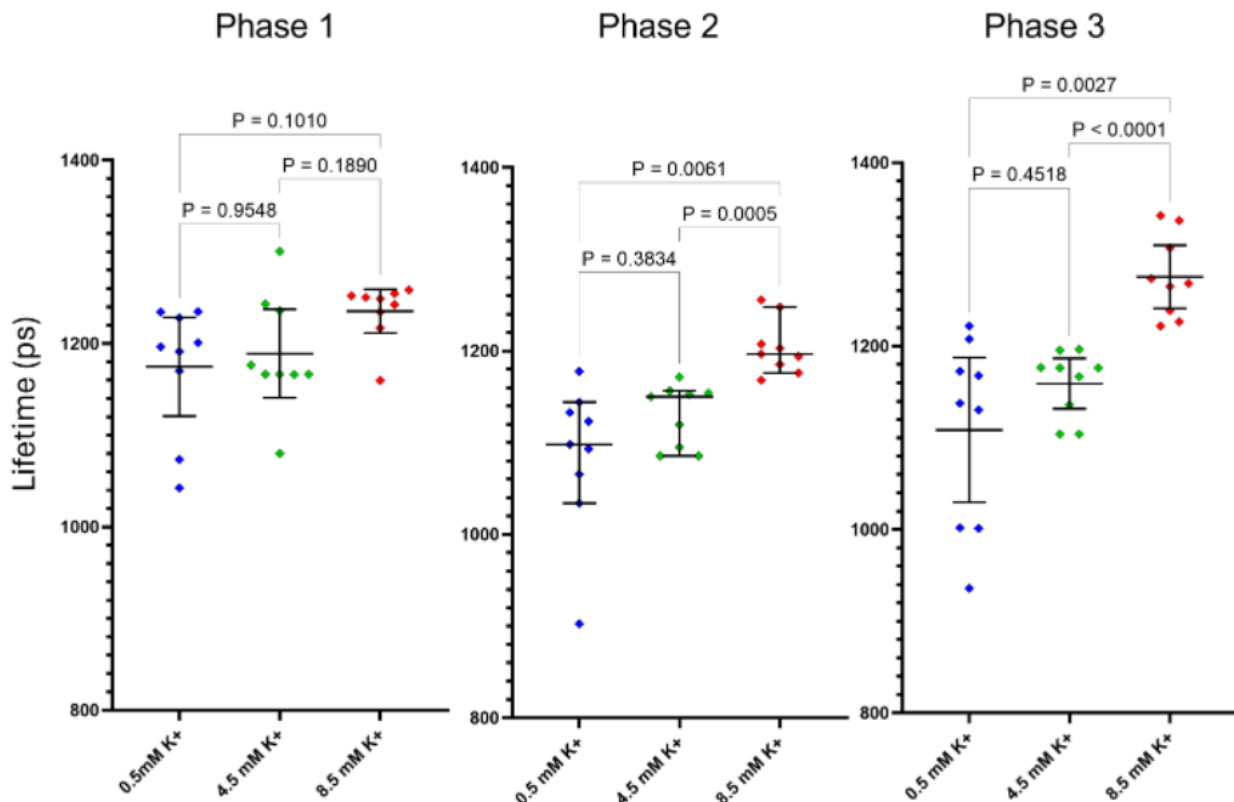


Figure 8: Comparing neural and neural crest bioelectricity:

Unlike in neurons (A) in which V_{mem} and calcium are closely linked, in neural crest cells (B) V_{mem} and calcium are largely separate pathways.

Supplemental Figures



Supplemental Figure 1: K⁺ has different effects on V_{mem}^{oe} at different phases of NCC migration. The 8.5mM K⁺ condition has elevated lifetime compared with the other two conditions in Phase 2 and 3, but not in Phase 1. Line at mean with 95% confidence interval.

Supplemental Tables

Supplemental Table 1: Glossary of imaging conditions

Figure Number	Imaging Conditions	Metadata
Figure 2 (all panels)	25X raised at 18°C overnight in 4.5mM K ⁺ , Imaged in 4.5mM K ⁺	MetaDataA_BeRST, MetaDataB_VF20CI
Figure 3 (all panels)	20X Overnight Timelapse	MetaDataC
Figure 4 (all panels)	20X Overnight Timelapse	MetaDataC
Figure 5 (all panels)	20X Overnight Timelapse	MetaDataC
Figure 6	20X Overnight Timelapse	MetaDataC
Figure 7A	20X Overnight Timelapse	MetaDataC
Figure 7B	20X Overnight Timelapse	MetaDataC
Figure 7,C	40X raised at 18°C overnight in 4.5mM K ⁺ , then moved to 0.5mM K ⁺ shortly prior to imaging	MetaDataD
Figure 7,D	40X raised at 18°C overnight in 4.5mM K ⁺ , then moved to 0.5mM K ⁺ shortly prior to imaging	MetaDataE
Supplemental Movie 1	20X Overnight Timelapse	MetaDataC
Supplemental Movie 2	40X raised at 18°C overnight in 4.5mM K ⁺ , then moved to 0.5mM K ⁺ shortly prior to imaging	MetaDataF
Supplemental Movie 3	40X raised at 18°C overnight in 4.5mM K ⁺ , then moved to 0.5mM K ⁺ shortly prior to imaging	MetaDataF
Supplemental Movie 4	20X Overnight Timelapse	MetaDataC
Supplemental Movie 5	20X Overnight Timelapse	MetaDataC
Supplemental Movie 6	20X Overnight Timelapse	MetaDataC
Supplemental Movie y	20X Overnight Timelapse	MetaDataC

Supplemental Table 1: Glossary of imaging conditions and imaging metafiles for each Figure and movie.

Supplemental Movie Legends:

Supplemental Movie 1: FLIM (Right) reveals bioelectric patterns at multiple timescales in migrating NC explants that are obscured by intensity only imaging. Fluorescent lifetime heatmap range displayed: 1.1ns to 1.3ns

Supplemental Movie 2: 40X magnification movie showing combined intensity and FLIM reveals diverse bioelectric dynamics of migrating NCCs. Fluorescent lifetime heatmap range displayed: 1 to 1.5 ns

Supplemental Movie 3: 40X magnification movie showing combined intensity and FLIM reveals diverse bioelectric dynamics of migrating NCCs. Fluorescent lifetime heatmap range displayed: 1 to 1.5 ns

Supplemental Movie 4: Optically estimated depolarization accompanying cell division. Colored nuclear ROI shows V_{mem}^{oe}, while extra-nuclear greyscale BeRST intensity shows cell morphology. Fluorescent lifetime heatmap range displayed: 1.1 to 1.4ns

Supplemental Movie 5: A cell departs the collective while hyperpolarizing, migrates independently, then depolarizes upon re-joining the collective. Fluorescent lifetime heatmap range displayed: 0.800ns to 1.400ns

Supplemental Movie 6: A group of cells hyperpolarizes and departs the collective, migrates as a separate collective, then depolarizes when re-contacting the larger collective. Fluorescent lifetime heatmap range displayed: 0.9 to 1.3ns

Supplemental Movie 7: Colored nuclear ROI shows V_{mem}^{oe} , while extra-nuclear greyscale BeRST intensity shows cell morphology. CellProfiler was used to identify nuclei and the dilate function was used to draw a one pixel thick black line surrounding them. Fluorescent lifetime heatmap range displayed: 0.9 to 1.3ns

References

1. Barbieri, M., *The organic codes. The basic mechanism of macroevolution*. Rivista di biologia, 1998. **91**(3): p. 481-513.
2. Barbieri, M., *Biosemiotics: a new understanding of life*. Die Naturwissenschaften, 2008. **95**(7): p. 577-99.
3. Barbieri, M., *A general model on the origin of biological codes*. Biosystems, 2019. **181**: p. 11-19.
4. Barbieri, M., *What is code biology?* Biosystems, 2018. **164**: p. 1-10.
5. Thompson, J., *The Decipherment of the Hieroglyphs*, in *Wonderful Things*. 2015, The American University in Cairo Press. p. 109-128.
6. Fields, C. and M. Levin, *Thoughts and thinkers: On the complementarity between objects and processes*. Physics of Life Reviews, 2025.
7. Levin, M., *Bioelectric networks: the cognitive glue enabling evolutionary scaling from physiology to mind*. Anim Cogn, 2023.
8. Salthe, S.N., *Cybersemiotics: Why Information Is Not Enough*. Biosemiotics, 2009. **2**(2): p. 247-253.
9. Lu, H.Y., et al., *Multi-scale neural decoding and analysis*. J Neural Eng, 2021. **18**(4).
10. Huth, A.G., et al., *Decoding the Semantic Content of Natural Movies from Human Brain Activity*. Front Syst Neurosci, 2016. **10**: p. 81.
11. Nishimoto, S., et al., *Reconstructing visual experiences from brain activity evoked by natural movies*. Current biology : CB, 2011. **21**(19): p. 1641-6.
12. Naselaris, T., et al., *Bayesian reconstruction of natural images from human brain activity*. Neuron, 2009. **63**(6): p. 902-15.
13. Prindle, A., et al., *Ion channels enable electrical communication in bacterial communities*. Nature, 2015. **527**(7576): p. 59-63.
14. Fields, C., J. Bischof, and M. Levin, *Morphological Coordination: A Common Ancestral Function Unifying Neural and Non-Neural Signaling*. Physiology, 2020. **35**(1): p. 16-30.
15. Fields, C. and M. Levin, *Competency in Navigating Arbitrary Spaces as an Invariant for Analyzing Cognition in Diverse Embodiments*. Entropy (Basel), 2022. **24**(6).
16. Pezzulo, G. and M. Levin, *Re-membering the body: applications of computational neuroscience to the top-down control of regeneration of limbs and other complex organs*. Integr Biol (Camb), 2015. **7**(12): p. 1487-517.
17. Levin, M., *Bioelectric signaling: Reprogrammable circuits underlying embryogenesis, regeneration, and cancer*. Cell, 2021. **184**(4): p. 1971-1989.
18. Harris, M.P., *Bioelectric signaling as a unique regulator of development and regeneration*. Development, 2021. **148**(10).
19. Bates, E., *Ion Channels in Development and Cancer*. Annu Rev Cell Dev Biol, 2015. **31**: p. 231-47.
20. Daley, M.C., et al., *The effects of membrane potential and extracellular matrix composition on vascular differentiation of cardiac progenitor cells*. Biochem Biophys Res Commun, 2020. **530**(1): p. 240-245.

21. Cao, L., et al., *Endogenous bioelectric currents promote differentiation of the mammalian lens*. J Cell Physiol, 2018. **233**(3): p. 2202-2212.
22. van Vliet, P., et al., *Hyperpolarization induces differentiation in human cardiomyocyte progenitor cells*. Stem Cell Rev, 2010. **6**(2): p. 178-85.
23. Konig, S., et al., *The calcineurin pathway links hyperpolarization (Kir2.1)-induced Ca²⁺ signals to human myoblast differentiation and fusion*. Development, 2006. **133**(16): p. 3107-14.
24. Konig, S., et al., *Membrane hyperpolarization triggers myogenin and myocyte enhancer factor-2 expression during human myoblast differentiation*. J Biol Chem, 2004. **279**(27): p. 28187-96.
25. Bhavsar, M.B., et al., *Role of Bioelectricity During Cell Proliferation in Different Cell Types*. Front Bioeng Biotechnol, 2020. **8**: p. 603.
26. Piggott, B.J., et al., *Paralytic, the Drosophila voltage-gated sodium channel, regulates proliferation of neural progenitors*. Genes Dev, 2019. **33**(23-24): p. 1739-1750.
27. Ding, F., et al., *Involvement of cationic channels in proliferation and migration of human mesenchymal stem cells*. Tissue & cell, 2012. **44**(6): p. 358-64.
28. Blackiston, D.J., K.A. McLaughlin, and M. Levin, *Bioelectric controls of cell proliferation: ion channels, membrane voltage and the cell cycle*. Cell Cycle, 2009. **8**(21): p. 3519-28.
29. Petsakou, A. and N. Perrimon, *Bioelectric regulation of intestinal stem cells*. Trends Cell Biol, 2022.
30. Thomas, C.F., et al., *Voltage-gated sodium channel activity mediates sea urchin larval skeletal patterning through spatial regulation of Wnt5 expression*. Development, 2023. **150**(10).
31. Pai, V.P., et al., *Genome-wide analysis reveals conserved transcriptional responses downstream of resting potential change in Xenopus embryos, axolotl regeneration, and human mesenchymal cell differentiation*. Regeneration (Oxf), 2016. **3**(1): p. 3-25.
32. Spannl, S., et al., *Glycolysis regulates Hedgehog signalling via the plasma membrane potential*. EMBO J, 2021. **40**(7): p. e107925.
33. Borodinsky, L.N. and Y.H. Belgacem, *Crosstalk among electrical activity, trophic factors and morphogenetic proteins in the regulation of neurotransmitter phenotype specification*. J Chem Neuroanat, 2016. **73**: p. 3-8.
34. Borodinsky, L.N., et al., *Spatiotemporal integration of developmental cues in neural development*. Dev Neurobiol, 2015. **75**(4): p. 349-59.
35. Belgacem, Y.H. and L.N. Borodinsky, *Inversion of Sonic hedgehog action on its canonical pathway by electrical activity*. Proc Natl Acad Sci U S A, 2015. **112**(13): p. 4140-5.
36. Pai, V.P., et al., *Transmembrane voltage potential controls embryonic eye patterning in Xenopus laevis*. Development (Cambridge, England), 2012. **139**(2): p. 313-323.
37. Bates, E., *Ion Channels in Development and Cancer*. Annual Review of Cell and Developmental Biology, 2015. **31**(1): p. 231-247.

38. Perathoner, S., et al., *Bioelectric signaling regulates size in zebrafish fins*. PLoS Genet, 2014. **10**(1): p. e1004080.
39. Pitcairn, E., et al., *Coordinating heart morphogenesis: A novel role for Hyperpolarization-activated cyclic nucleotide-gated (HCN) channels during cardiogenesis in Xenopus laevis*. Communicative & Integrative Biology, 2017. **10**(3): p. e1309488.
40. Pai, V.P., et al., *Endogenous Gradients of Resting Potential Instructively Pattern Embryonic Neural Tissue via Notch Signaling and Regulation of Proliferation*. The Journal of Neuroscience, 2015. **35**(10): p. 4366-85.
41. Adams, D.S., et al., *Bioelectric signalling via potassium channels: a mechanism for craniofacial dysmorphogenesis in KCNJ2-associated Andersen-Tawil Syndrome*. J Physiol, 2016. **594**(12): p. 3245-3270.
42. Vandenberg, L.N., R.D. Morrie, and D.S. Adams, *V-ATPase-dependent ectodermal voltage and pH regionalization are required for craniofacial morphogenesis*. Dev Dyn, 2011. **240**(8): p. 1889-904.
43. Daane, J.M., et al., *Modulation of bioelectric cues in the evolution of flying fishes*. Current Biology, 2021. **31**(22): p. 5052-5061.e8.
44. Tseng, A.S., et al., *Induction of vertebrate regeneration by a transient sodium current*. J Neurosci, 2010. **30**(39): p. 13192-200.
45. Adams, D.S., A.S. Tseng, and M. Levin, *Light-activation of the Archaeorhodopsin H(+) pump reverses age-dependent loss of vertebrate regeneration: sparking system-level controls in vivo*. Biol Open, 2013. **2**(3): p. 306-13.
46. Pai, V.P. and M. Levin, *HCN2 channel-induced rescue of brain, eye, heart and gut teratogenesis caused by nicotine, ethanol and aberrant notch signalling*. Wound Repair Regen, 2022. **30**(6): p. 681-706.
47. Chernet, B.T. and M. Levin, *Transmembrane voltage potential is an essential cellular parameter for the detection and control of tumor development in a Xenopus model*. Disease models & mechanisms, 2013. **6**(3): p. 595-607.
48. Chernet, B.T., C. Fields, and M. Levin, *Long-range gap junctional signaling controls oncogene-mediated tumorigenesis in Xenopus laevis embryos*. Front Physiol, 2014. **5**: p. 519.
49. Lobikin, M., et al., *Resting potential, oncogene-induced tumorigenesis, and metastasis: the bioelectric basis of cancer in vivo*. Phys Biol, 2012. **9**(6): p. 065002.
50. Chernet, B.T., et al., *Use of genetically encoded, light-gated ion translocators to control tumorigenesis*. Oncotarget, 2016. **7**(15): p. 19575-19588.
51. Balasubramanian, S., et al., *Electroceuticals: emerging applications beyond the nervous system and excitable tissues*. Trends in Pharmacological Sciences, 2024. **45**(5): p. 391-394.
52. Kofman, K. and M. Levin, *Bioelectric pharmacology of cancer: A systematic review of ion channel drugs affecting the cancer phenotype*. Prog Biophys Mol Biol, 2024. **191**: p. 25-39.
53. Levin, M. and C.J. Martyniuk, *The bioelectric code: An ancient computational medium for dynamic control of growth and form*. Biosystems, 2018. **164**: p. 76-93.

54. Hotary, K.B. and K.R. Robinson, *Endogenous electrical currents and the resultant voltage gradients in the chick embryo*. Dev Biol, 1990. **140**(1): p. 149-60.
55. Robinson, K.R., *The responses of cells to electrical fields: a review*. J Cell Biol, 1985. **101**(6): p. 2023-7.
56. Cooper, M.S. and R.E. Keller, *Perpendicular orientation and directional migration of amphibian neural crest cells in DC electrical fields*. Proc Natl Acad Sci U S A, 1984. **81**(1): p. 160-4.
57. Stump, R.F. and K.R. Robinson, *Xenopus neural crest cell migration in an applied electrical field*. Journal of Cell Biology, 1983. **97**(4): p. 1226-1233.
58. Bronner-Fraser, M., *Neural crest cell migration in the developing embryo*. Trends Cell Biol, 1993. **3**(11): p. 392-7.
59. Trainor, P.A., *Making headway: the roles of Hox genes and neural crest cells in craniofacial development*. ScientificWorldJournal, 2003. **3**: p. 240-64.
60. Mayor, R. and M.J. Aybar, *Induction and development of neural crest in Xenopus laevis*. Cell Tissue Res, 2001. **305**(2): p. 203-9.
61. Fuchs, S. and L. Sommer, *The neural crest: understanding stem cell function in development and disease*. Neurodegener Dis, 2007. **4**(1): p. 6-12.
62. Lo, C.W., et al., *Cx43 gap junction gene expression and gap junctional communication in mouse neural crest cells*. Dev Genet, 1997. **20**(2): p. 119-32.
63. Lo, C.W., K.L. Waldo, and M.L. Kirby, *Gap junction communication and the modulation of cardiac neural crest cells*. Trends Cardiovasc Med, 1999. **9**(3-4): p. 63-9.
64. Stump, R.F. and K.R. Robinson, *Xenopus neural crest cell migration in an applied electrical field*. J Cell Biol, 1983. **97**(4): p. 1226-33.
65. Gruler, H. and R. Nuccitelli, *Neural crest cell galvanotaxis: new data and a novel approach to the analysis of both galvanotaxis and chemotaxis*. Cell Motil Cytoskeleton, 1991. **19**(2): p. 121-33.
66. Adams, D.S., et al., *Bioelectric signalling via potassium channels: a mechanism for craniofacial dysmorphogenesis in KCNJ2-associated Andersen-Tawil Syndrome*. J Physiol, 2016. **594**(12): p. 3245-70.
67. Belus, M.T., et al., *Kir2.1 is important for efficient BMP signaling in mammalian face development*. Dev Biol, 2018. **444 Suppl 1**(Suppl 1): p. S297-s307.
68. Melchionda, M., et al., *Ca²⁺/H⁺ exchange by acidic organelles regulates cell migration in vivo*. J Cell Biol, 2016. **212**(7): p. 803-13.
69. Canales Coutiño, B. and R. Mayor, *The mechanosensitive channel Piezo1 cooperates with semaphorins to control neural crest migration*. Development, 2021. **148**(23).
70. Shellard, A. and R. Mayor, *Rules of collective migration: from the wildebeest to the neural crest*. Philos Trans R Soc Lond B Biol Sci, 2020. **375**(1807): p. 20190387.
71. Barriga, E.H. and E. Theveneau, *In vivo Neural Crest Cell Migration Is Controlled by "Mixotaxis"*. Frontiers in Physiology, 2020. **11**.
72. Theveneau, E. and C. Linker, *Leaders in collective migration: are front cells really endowed with a particular set of skills?* F1000Res, 2017. **6**: p. 1899.

73. Theveneau, E., et al., *Chase-and-run between adjacent cell populations promotes directional collective migration*. Nat Cell Biol, 2013. **15**(7): p. 763-72.
74. Theveneau, E. and R. Mayor, *Can mesenchymal cells undergo collective cell migration? The case of the neural crest*. Cell Adhesion and Migration, 2011. **5**(6): p. 490-498.
75. Theveneau, E. and R. Mayor, *Collective cell migration of the cephalic neural crest: the art of integrating information*. Genesis, 2011. **49**(4): p. 164-76.
76. Hartmann, J. and R. Mayor, *Self-organized collective cell behaviors as design principles for synthetic developmental biology*. Semin Cell Dev Biol, 2023. **141**: p. 63-73.
77. Theveneau, E., et al., *Collective Chemotaxis Requires Contact-Dependent Cell Polarity*. Developmental Cell, 2010. **19**(1): p. 39-53.
78. Shellard, A., et al., *Supracellular contraction at the rear of neural crest cell groups drives collective chemotaxis*. Science, 2018. **362**(6412): p. 339-343.
79. James, W., *The principles of psychology, Vol I*. The principles of psychology, Vol I. 1890, New York, NY, US: Henry Holt and Co. xii, 697-xii, 697.
80. Couly, G., et al., *The regeneration of the cephalic neural crest, a problem revisited: the regenerating cells originate from the contralateral or from the anterior and posterior neural fold*. Development, 1996. **122**(11): p. 3393-407.
81. Le Douarin, N.M., et al., *Neural crest cell plasticity and its limits*. Development, 2004. **131**(19): p. 4637-50.
82. Little, G.E., et al., *Specificity and plasticity of thalamocortical connections in Sema6A mutant mice*. PLoS Biol, 2009. **7**(4): p. e98.
83. Zarzosa, A., et al., *Axolotls with an under- or oversupply of neural crest can regulate the sizes of their dorsal root ganglia to normal levels*. Dev Biol, 2014. **394**(1): p. 65-82.
84. Mitsiadis, T.A., et al., *Development of teeth in chick embryos after mouse neural crest transplantations*. Proc Natl Acad Sci U S A, 2003. **100**(11): p. 6541-5.
85. McMillen, P. and M. Levin, *Collective intelligence: A unifying concept for integrating biology across scales and substrates*. Commun Biol, 2024. **7**(1): p. 378.
86. Vicente-Manzanares, M., et al., *Non-muscle myosin II takes centre stage in cell adhesion and migration*. Nature Reviews Molecular Cell Biology, 2009. **10**(11): p. 778-790.
87. Lazzari-Dean, J.R., A.M.M. Gest, and E.W. Miller, *Measuring Absolute Membrane Potential Across Space and Time*. Annu Rev Biophys, 2021. **50**: p. 447-468.
88. Adams, D.S. and M. Levin, *Measuring resting membrane potential using the fluorescent voltage reporters DiBAC4(3) and CC2-DMPE*. Cold Spring Harbor protocols, 2012. **2012**(4): p. 459-64.
89. Adams, D.S. and M. Levin, *General principles for measuring resting membrane potential and ion concentration using fluorescent bioelectricity reporters*. Cold Spring Harbor protocols, 2012. **2012**(4): p. 385-97.
90. Smetters, D., A. Majewska, and R. Yuste, *Detecting action potentials in neuronal populations with calcium imaging*. Methods, 1999. **18**(2): p. 215-21.

91. Yuste, R. and L.C. Katz, *Control of postsynaptic Ca²⁺ influx in developing neocortex by excitatory and inhibitory neurotransmitters*. *Neuron*, 1991. **6**(3): p. 333-44.
92. McMillen, P., R. Novak, and M. Levin, *Toward Decoding Bioelectric Events in Xenopus Embryogenesis: New Methodology for Tracking Interplay Between Calcium and Resting Potentials In Vivo*. *J Mol Biol*, 2020. **432**(2): p. 605-620.
93. George, L.F. and E.A. Bates, *Mechanisms Underlying Influence of Bioelectricity in Development*. *Frontiers in Cell and Developmental Biology*, 2022. **10**.
94. Levin, M., G. Pezzulo, and J.M. Finkelstein, *Endogenous Bioelectric Signaling Networks: Exploiting Voltage Gradients for Control of Growth and Form*. *Annu Rev Biomed Eng*, 2017. **19**: p. 353-387.
95. Lazzari-Dean, J.R., A.M.M. Gest, and E.W. Miller, *Optical estimation of absolute membrane potential using fluorescence lifetime imaging*. *eLife*, 2019. **8**: p. e44522.
96. Lazzari-Dean, J.R. and E.W. Miller, *Optical Estimation of Absolute Membrane Potential Using One- and Two-Photon Fluorescence Lifetime Imaging Microscopy*. *Bioelectricity*, 2021. **3**(3): p. 197-203.
97. Huang, Y.L., A.S. Walker, and E.W. Miller, *A Photostable Silicon Rhodamine Platform for Optical Voltage Sensing*. *Journal of the American Chemical Society*, 2015. **137**(33): p. 10767-10776.
98. Shannon, C.E., *A Mathematical Theory of Communication*. *Bell System Technical Journal*, 1948. **27**(3): p. 379-423.
99. McMillen, P., S.I. Walker, and M. Levin, *Information Theory as an Experimental Tool for Integrating Disparate Biophysical Signaling Modules*. *Int J Mol Sci*, 2022. **23**(17).
100. Jekely, G., F. Keijzer, and P. Godfrey-Smith, *An option space for early neural evolution*. *Philos Trans R Soc Lond B Biol Sci*, 2015. **370**(1684).
101. de Wiljes, O.O., et al., *Modeling spontaneous activity across an excitable epithelium: Support for a coordination scenario of early neural evolution*. *Front Comput Neurosci*, 2015. **9**: p. 110.
102. Keijzer, F., M. van Duijn, and P. Lyon, *What nervous systems do: early evolution, input-output, and the skin brain thesis*. *Adaptive Behavior*, 2013. **21**(2): p. 67-85.
103. Zhang, Y., et al., *Fast and sensitive GCaMP calcium indicators for imaging neural populations*. *Nature*, 2023. **615**(7954): p. 884-891.
104. Toettcher, J.E., O.D. Weiner, and W.A. Lim, *Using optogenetics to interrogate the dynamic control of signal transmission by the Ras/Erk module*. *Cell*, 2013. **155**(6): p. 1422-34.
105. Goedhart, J., et al., *Structure-guided evolution of cyan fluorescent proteins towards a quantum yield of 93%*. *Nat Commun*, 2012. **3**: p. 751.
106. Gouignard, N., C. Rouvière, and E. Theveneau, *Using Xenopus Neural Crest Explants to Study Epithelial-Mesenchymal Transition*, in *The Epithelial-to Mesenchymal Transition: Methods and Protocols*, K. Campbell and E. Theveneau, Editors. 2021, Springer US: New York, NY. p. 257-274.
107. Sater, A.K., R.A. Steinhardt, and R. Keller, *Induction of neuronal differentiation by planar signals in Xenopus embryos*. *Dev Dyn*, 1993. **197**(4): p. 268-80.
108. Schindelin, J., et al., *Fiji: an open-source platform for biological-image analysis*. *Nat Methods*, 2012. **9**(7): p. 676-82.

109. Stirling, D.R., et al., *CellProfiler 4: improvements in speed, utility and usability*. BMC Bioinformatics, 2021. **22**(1): p. 433.
110. Lamprecht, M.R., D.M. Sabatini, and A.E. Carpenter, *CellProfiler: free, versatile software for automated biological image analysis*. Biotechniques, 2007. **42**(1): p. 71-5.
111. Moore, D. and P. McMillen, *CAIM: information analysis of imaging data*. 2019.
112. Lazic, S.E., C.J. Clarke-Williams, and M.R. Munafò, *What exactly is 'N' in cell culture and animal experiments?* PLoS Biol, 2018. **16**(4): p. e2005282.
113. Lord, S.J., et al., *SuperPlots: Communicating reproducibility and variability in cell biology*. Journal of Cell Biology, 2020. **219**(6).
114. Motulsky, H.J. *GraphPad Statistics Guide*. [cited 2025 March 4]; Available from: <https://www.graphpad.com/guides/prism/latest/statistics/index.htm>.
115. McMillen, P. and M. Levin, *Optical Estimation of Bioelectric Patterns in Living Embryos*. Methods Mol Biol, 2024. **2745**: p. 91-102.
116. Bonzanni, M., et al., *Defined extracellular ionic solutions to study and manipulate the cellular resting membrane potential*. Biology Open, 2020. **9**(1).
117. Brodskiy, P.A. and J.J. Zartman, *Calcium as a signal integrator in developing epithelial tissues*. Phys Biol, 2018. **15**(5): p. 051001.
118. Brodskiy, P.A., et al., *Decoding Calcium Signaling Dynamics during Drosophila Wing Disc Development*. Biophys J, 2019. **116**(4): p. 725-740.
119. Alivisatos, A.P., et al., *The brain activity map project and the challenge of functional connectomics*. Neuron, 2012. **74**(6): p. 970-4.
120. McKinney, M.C. and P.M. Kulesa, *In vivo calcium dynamics during neural crest cell migration and patterning using GCaMP3*. Dev Biol, 2011. **358**(2): p. 309-17.
121. McKinney, M.C., et al., *Neural crest cell communication involves an exchange of cytoplasmic material through cellular bridges revealed by photoconversion of KikGR*. Dev Dyn, 2011. **240**(6): p. 1391-401.
122. Xu, X., et al., *N-cadherin and Cx43alpha1 gap junctions modulates mouse neural crest cell motility via distinct pathways*. Cell Commun Adhes, 2001. **8**(4-6): p. 321-4.
123. Barghouth, P.G., M. Thiruvalluvar, and N.J. Oviedo, *Bioelectrical regulation of cell cycle and the planarian model system*. Biochimica et biophysica acta, 2015. **1848**(10 Pt B): p. 2629-37.
124. Aprea, J. and F. Calegari, *Bioelectric state and cell cycle control of mammalian neural stem cells*. Stem cells international, 2012. **2012**: p. 816049.
125. Blackiston, D.J., K.A. McLaughlin, and M. Levin, *Bioelectric controls of cell proliferation: Ion channels, membrane voltage and the cell cycle*. Cell Cycle, 2009. **8**(21): p. 3527-3536.
126. Wang, X., et al., *Animal cells connected by nanotubes can be electrically coupled through interposed gap-junction channels*. Proc Natl Acad Sci U S A, 2010. **107**(40): p. 17194-9.
127. Teddy, J.M. and P.M. Kulesa, *In vivo evidence for short- and long-range cell communication in cranial neural crest cells*. Development, 2004. **131**(24): p. 6141-51.

128. Wang, X. and H.H. Gerdes, *Long-distance electrical coupling via tunneling nanotubes*. *Biochim Biophys Acta*, 2012. **1818**(8): p. 2082-6.
129. McMillen, P., et al., *Beyond Neurons: Long Distance Communication in Development and Cancer*. *Front Cell Dev Biol*, 2021. **9**: p. 739024.
130. Osswald, M., et al., *Brain tumour cells interconnect to a functional and resistant network*. *Nature*, 2015. **528**(7580): p. 93-8.
131. Osswald, M., et al., *A malignant cellular network in gliomas: potential clinical implications*. *Neuro Oncol*, 2016. **18**(4): p. 479-85.
132. Weil, S., et al., *Tumor microtubes convey resistance to surgical lesions and chemotherapy in gliomas*. *Neuro Oncol*, 2017. **19**(10): p. 1316-1326.
133. Keijzer, F. and A. Arnellos, *The animal sensorimotor organization: a challenge for the environmental complexity thesis*. *Biol Philos*, 2017. **32**(3): p. 421-441.
134. Pai, V.P. and M. Levin, *HCN2 channel-induced rescue of brain, eye, heart and gut teratogenesis caused by nicotine, ethanol and aberrant notch signalling*. *Wound Repair Regen*, 2022.
135. Pai, V.P., et al., *HCN2 Channel-Induced Rescue of Brain Teratogenesis via Local and Long-Range Bioelectric Repair*. *Frontiers in Cellular Neuroscience*, 2020. **14**(136): p. 136.
136. Ebrahimkhani, M.R. and M. Levin, *Synthetic living machines: A new window on life*. *iScience*, 2021. **24**(5): p. 102505.
137. Levin, M., *The Multiscale Wisdom of the Body: Collective Intelligence as a Tractable Interface for Next-Generation Biomedicine*. *Bioessays*, 2024: p. e202400196.
138. Whited, J.L. and M. Levin, *Bioelectrical controls of morphogenesis: from ancient mechanisms of cell coordination to biomedical opportunities*. *Curr Opin Genet Dev*, 2019. **57**: p. 61-69.
139. Ding, F., et al., *Changes in the composition of brain interstitial ions control the sleep-wake cycle*. *Science*, 2016. **352**(6285): p. 550-5.
140. Purvis, J.E. and G. Lahav, *Encoding and decoding cellular information through signaling dynamics*. *Cell*, 2013. **152**(5): p. 945-56.
141. Johnson, H.E. and J.E. Toettcher, *Signaling Dynamics Control Cell Fate in the Early Drosophila Embryo*. *Dev Cell*, 2019. **48**(3): p. 361-370 e3.
142. Wilson, M.Z., et al., *Tracing Information Flow from Erk to Target Gene Induction Reveals Mechanisms of Dynamic and Combinatorial Control*. *Mol Cell*, 2017. **67**(5): p. 757-769 e5.
143. Goglia, A.G., et al., *A Live-Cell Screen for Altered Erk Dynamics Reveals Principles of Proliferative Control*. *Cell Syst*, 2020. **10**(3): p. 240-253 e6.
144. Rühl, P., et al., *An Ultrasensitive Genetically Encoded Voltage Indicator Uncovers the Electrical Activity of Non-Excitable Cells*. *Advanced Science*, 2024. **11**(20): p. 2307938.
145. Pai, V.P., et al., *HCN2 Channel-Induced Rescue of Brain Teratogenesis via Local and Long-Range Bioelectric Repair*. *Frontiers in Cellular Neuroscience*, 2020. **14**(136).
146. Pitcairn, E., et al., *Coordinating heart morphogenesis: A novel role for hyperpolarization-activated cyclic nucleotide-gated (HCN) channels during cardiogenesis in Xenopus laevis*. *Commun Integr Biol*, 2017. **10**(3): p. e1309488.

147. Johard, H., et al., *HCN Channel Activity Balances Quiescence and Proliferation in Neural Stem Cells and Is a Selective Target for Neuroprotection During Cancer Treatment*. Mol Cancer Res, 2020. **18**(10): p. 1522-1533.
148. Lau, Y.T., et al., *Effects of hyperpolarization-activated cyclic nucleotide-gated (HCN) channel blockers on the proliferation and cell cycle progression of embryonic stem cells*. Pflugers Archiv : European journal of physiology, 2011. **461**(1): p. 191-202.
149. Bruzauskaite, I., et al., *Relevance of HCN2-expressing human mesenchymal stem cells for the generation of biological pacemakers*. Stem Cell Res Ther, 2016. **7**(1): p. 67.
150. Benarroch, E.E., *HCN channels: function and clinical implications*. Neurology, 2013. **80**(3): p. 304-10.
151. Depuydt, A.S., S. Peigneur, and J. Tytgat, *Review: HCN Channels in the Heart*. Curr Cardiol Rev, 2022. **18**(4): p. e040222200836.
152. Stevens, S.M. and W.T. Pu, *HCN4 charges up the first heart field*. Circulation research, 2013. **113**(4): p. 350-1.
153. Barbieri, M., *The definitions of information and meaning two possible boundaries between physics and biology*. Riv Biol, 2004. **97**(1): p. 91-109.
154. Salthe, S.N., *Hierarchy. More Developed Sign: Interpreting the Work of Jesper Hoffmeyer*, 2012. **10**: p. 155-156.
155. Salthe, S.N., *The System of Interpretance, Naturalizing Meaning as Finality*. Biosemiotics, 2008. **1**(3): p. 285-294.
156. Ó Nualláin, S., *Subjects and Objects: Metaphysics, Biology, Consciousness, and Cognition*. Biosemiotics, 2008. **1**(2): p. 239-251.
157. Kauffman, S. and P. Clayton, *On emergence, agency, and organization*. Biology & Philosophy, 2006. **21**(4): p. 501-521.
158. Salthe, S.N., *Semiosis as development*. Joint Conference on the Science and Technology of Intelligent Systems, 1998: p. 730-735.

